Accepted Manuscript

Decimeter-scale mapping of carbonate-controlled trace element distribution in Neoarchean cuspate stromatolites

Matthew R. Warke, Nicholas P. Edwards, Roy A. Wogelius, Phillip L. Manning, Uwe Bergmann, Victoria M. Egerton, Katalina C. Kimball, Russell J. Garwood, Nicolas J. Beukes, Stefan Schröder

Decimeter-scale mapping of carbonate-controlled trace element distribution in Neoarchean cuspate stromatolites

Matthew R. Warke[1,2*], Nicholas P. Edwards[3,4,5], Roy A. Wogelius[3,4], Phillip L. Manning[3], Uwe Bergmann[6], Victoria M. Egerton[3], Katalina C. Kimball[6], Russell J. Garwood[3,7], Nicolas J. Beukes[8] and Stefan Schröder[1]

[1]Basin Studies and Petroleum Geoscience, School of Earth and Environmental Sciences, University of Manchester, Manchester M13 9PL, United Kingdom

[2]School of Earth and Environmental Sciences, University of St Andrews, St Andrews, KY16 9AL, United Kingdom;*corresponding author: mw438@st-andrews.ac.uk

[3]Interdisciplinary Centre for Ancient Life, School of Earth and Environmental Sciences, University of Manchester, Manchester M13 9PL, UK

[4]Williamson Research Centre for Molecular Environmental Science, School of Earth and Environmental Sciences, University of Manchester, Manchester M13 9PL, UK

[5]SLAC National Accelerator Laboratory, Menlo Park, CA, 94025, USA

[6]Stanford PULSE Institute, SLAC National Accelerator Laboratory, Menlo Park, CA, 94025, USA

[7]Earth Sciences Department, Natural History Museum, London SW7 5BD, UK.

[8]DST-NRF CIMERA, Department of Geology, University of Johannesburg, PO Box 524, Auckland Park, 2000, South Africa

Ancient stromatolites can provide key insights into the early evolution of life on Earth. Neoarchean fenestrate stromatolites from the ~2520 Ma Upper Nauga Formation (Transvaal Supergroup, South Africa) preserve cuspate morphologies. They possess clearly delineated support and drape structures interpreted as dolomitized microbial mat material. Petrographic observations show that the biogenic structures are composed of planar-s to non-planar ferroan dolomite, encased in ferroan calcite, including herringbone calcite textures. The cuspate stromatolites were analyzed using Synchrotron Rapid Scanning X-Ray Fluorescence (SRS-XRF) and more conventional techniques to determine: (i) whether element distributions could be distinguished in ancient stromatolites at both cm to dm scales, (ii) whether element distributions show variation between biogenic and abiogenic textures, and (iii) the sample's paragenesis. The distributions of Ca, Fe, Mn, Pb, Cu, As, Br, Al, Si, P, and S directly correspond to dolomitized stromatolitic structures and show trace element distributions are principally controlled by calcite and dolomite occurrence. Dolomite formation was mainly driven by seawater-derived fluids given the high concentrations of Fe and retention of marine shale-normalized rare earth element and yttrium (REY$_{SN}$) patterns, however the spatial association of dolomite to stromatolite structures may reflect microbially-influenced mineral nucleation. Given the complexity of this sample's paragenetic evolution, trace metal distributions cannot be conclusively tied to specific metabolic pathways, bioaccumulation or passive binding, however, the results show SRS-XRF can be used for quantifiable, spatial, *in-situ* investigation of ancient microbialites.

1. Introduction

The early Paleoproterozoic rise in oxygen – including the period from ~2410-2310 Ma known as the "Great Oxidation Event" (GOE; Holland, 2002; 2006; Bekker et al., 2004; Johnson et al., 2013; Luo et al., 2016) – marks one of the first steps in the gradational oxygenation of Earth's atmosphere. The GOE is closely associated with (and sometimes defined as) the disappearance of mass-independently fractionated sulfur isotopes from the rock record, which reflects a rise in the concentration of atmospheric oxygen (Farquhar et al., 2000; Guo et al., 2009; Luo et al., 2016).

As the only probable source of free oxygen was as a byproduct of oxygenic photosynthesis by cyanobacteria, understanding the timing and rate of the GOE depends upon constraining the earliest direct and trace evidence of cyanobacteria (Lyons et al., 2014).

Studies of pre-GOE successions suggest that trace amounts of free oxygen were being produced as early as the late Neoarchean, particularly on shallow-water carbonate platforms, such as the Campbellrand Subgroup (Transvaal Supergroup, South Africa; Beukes, 1987; Wille et al., 2007; Garvin et al, 2009; Voegelin et al., 2010). Trace levels of oxygen imply that cyanobacteria capable of performing oxygenic photosynthesis emerged by or prior to ~2700 Ma (Canfield, 2005; Lyons et al., 2014; Butterfield, 2015; Schirrmeister et al., 2016). However, others have argued that oxygenic photosynthesis developed later (after ~2400 Ma), and that its evolution in cyanobacteria led directly to the GOE (Kirschvink and Kopp, 2008; Johnson et al., 2013; Fischer et al., 2016).

Seeking independent constraints on the timing of cyanobacterial emergence from the Neoarchean to Paleoproterozoic microfossil record is problematic because of its sparsity and ambiguity (Butterfield, 2015; Schirrmeister et al., 2016). Some of the earliest proposed cyanobacterial microfossils are described from the Campbellrand Subgroup, in which cherty and dolomitic facies of the Gamohaan Formation contain filamentous *Siphonophycus transvaalensis* microfossils (Klein et al., 1987). The Gamohaan Formation has been dated to the late Neoarchean – 2521 ± 3 Ma (Sumner and Bowring, 1996) and 2516 ± 4 (Altermann and Nelson, 1998) – and therefore these microfossils are considered to be examples of Neoarchean cyanobacteria (Wright, 2000; Wright and Altermann, 2000; Butterfield, 2015; Schirrmeister et al., 2016). Elsewhere in the Gamohaan Formation large, smooth coccoid microfossils, coupled with the multiple sulfur isotope systematics of pyrite in the formation suggest the presence of sulfur-oxidizing bacteria (Czaja et al., 2016). In the distally (and temporally) equivalent Nauga Formation, microfossils of benthic coccoid cyanobacteria have also been described (Kazmierczak and Altermann, 2002; Kazmierczak et al., 2009). However, this microfossil record remains debated (Fischer et al., 2016); specifically, the biogenicity of filamentous structures has been disputed (Brasier et al., 2002; 2005).

With so few Neoarchean microfossils known, attempts have been made to infer the presence of cyanobacteria indirectly. Molecular biomarkers, such as 2 α-methylhopane (Brocks et al., 1999; Summons et al., 1999) are unreliable, being susceptible to sample contamination (Rasmussen et al.,

2008; French et al., 2015). A more common approach has been to search for the unique fingerprint (and waste product) of the oxygenic cyanobacterial metabolism: oxygen (Farquhar et al., 2011; Lyons et al., 2014; Fischer et al., 2016).

It has been proposed that heterogeneous element distributions within microbialites may also serve as a biosignature for past microbial life (Lepot et al 2008; 2009). Microbial metabolisms may concentrate certain metals via passive processes (Sforna et al., 2017), although in modern analogues the precise mechanism by which this may (or may not) occur is debated (Webster-Brown and Webster, 2007).

This contribution tests a new method to quantify such heterogeneities by determining the spatial distribution of large-scale chemistry (centimeter to decimeter scale) in ancient stromatolites using Synchrotron Rapid Scanning X-Ray Fluorescence (SRS-XRF). SRS-XRF is a non-destructive imaging technique that is capable of mapping geochemical variation across large samples (100 x 100 x 30 cm) at a scan rate of approximately 30 s.cm^{-2}, yielding faster large scans that retain high resolution (20-100 micron) and sensitivity (ppm) than can be achieved using conventional synchrotron and lab benchtop techniques (e.g. Sforna et al., 2017) or electron microprobe (Bergmann et al., 2010; Edwards et al., 2013). SRS-XRF scans of paleontological specimens have revealed discrete chemical inventories at the decimeter-scale, giving insight to the endogeneity of elemental distributions within fossilized bone, skin, feathers, and plant tissues that are derived from specific biosynthetic pathways – such as photosynthesis – and which have been preserved despite burial and diagenesis (Bergmann et al., 2010; 2012; Edwards et al, 2011; 2014; Wogelius et al., 2011; Manning et al., 2013).

The high-resolution trace element maps generated are then interpreted in the context of complimentary petrographic and geochemical datasets to ascertain whether the observed element distributions can be attributed to microbial and/or diagenetic processes. As such, it is proposed that SRS-XRF analysis constitutes a new approach that is capable of deciphering larger scale depositional and diagenetic processes that have affected microbialites while also highlighting areas of interest for higher resolution studies of past microbial life.

2. Background information

2.1 Geological setting

The Campbellrand-Malmani carbonate platform was deposited between ~2583 and 2521 Ma on the Kaapvaal Craton in South Africa (Figure 1; Martin et al., 1998; Sumner and Beukes, 2006). The more proximal environments occur in the Transvaal sub-basin, whereas the Griqualand West sub-basin preserves platform margin to slope facies (Figure 1; Beukes 1987; Sumner and Bowring, 1996). The Nauga Formation (Figure 2) is a slope succession that largely consists of stacked microbialite cycles (Figure 3), including a large proportion of fenestrate stromatolites (Sumner, 1997; 2000; Schröder et al., 2009). The platform top (temporal) equivalent of the Nauga Formation is the Gamohaan Formation

(Figure 2; Sumner and Beukes, 2006). Both units were deposited during the initial phase of a platform-drowning transgression which ultimately led to the deposition of the iron-formations of the overlying Asbesheuwels Subgroup (Figure 2; Klein and Beukes, 1989; Sumner and Bowring, 1996; Sumner and Beukes, 2006).

Lithofacies containing stromatolites were deposited in a sub-tidal, low energy, open-marine environment lacking significant detrital input (Sumner, 1997; Sumner and Grotzinger, 2004; Sumner and Beukes, 2006); carbonates precipitated directly from seawater (Sumner, 1997). Nauga and Gamohaan Formation limestones are well preserved as the Campbellrand Subgroup has only experienced sub-greenschist burial conditions (Sumner, 1997). Maximum burial temperatures are estimated to between 250 and 330 °C (Ergolu et al., 2017; 2018). Fabric destructive dolomitization is noted on the Campbellrand platform (Sumner, 1997), however the sample selected for this study is predominantly limestone and comes from a portion of the core GKF01 which was not dolomitized in this manner (Schröder et al., 2006).

2.2 Cuspate stromatolites

Fenestrate stromatolites are a class of laminated lithified structures (stromatolites) with morphologies falling on a continuum between three end-members: (i) cuspate, (ii) net-like, and (iii) tented (Sumner, 1997; 2000). Net-like and tented stromatolites are known from the Fairfield Formation of the Campbellrand Subgroup (~2.5 Ga; Beukes, 1987; Sumner, 2000). Cuspate stromatolites were first described from the Gamohaan and Nauga formations (Beukes, 1987; Sumner, 1997). They are also known from the Neoarchean Bulawayo Greenstone Belt (~2.6 Ga; Sumner and Grotzinger, 1996) and Carawine Formation of the Hamersley Group, Australia (~2.6 Ga; Rasmussen et al., 2005; Murphy and Sumner, 2008), in addition to the Mesoproterozoic Sulky Formation of the Dismal Lakes Group, Canada (~1.66-1.27 Ga; Bowring and Ross, 1985; Le Cheminant and Heaman, 1989; Bartley et al., 2014). Cuspate stromatolites are divided into three morphological components: (i) vertical supports, (ii) sub-horizontal draping structures, which are commonly concave upwards, and (iii) lunate void-filling carbonate cements (Figure 3; Sumner, 1997; 2000; Bartley et al., 2014). Cuspate stromatolites in the Nauga Formation have been very locally dolomitized; previous studies have either not proposed dolomitization mechanisms (Sumner 1997; 2000) or have argued that dolomitization may have been driven by microbial activity, particularly microbial sulfate reduction (Wright, 2000; Wright and Altermann, 2000).

In the Gamohaan/Nauga Formation it was originally proposed that the unusual cuspate morphology may result from the upward, phototactic growth of motile, filamentous cyanobacteria (Beukes, 1987). A biological origin for these structures has long been inferred, supported by their retention of organic carbon within the cuspate structures (Sumner, 1997). A biological origin is also supported by the preservation of filamentous microfossils of *Siphonophycus transvaalensis* (Klein et al., 1987) which are

reported from within the cuspate structures themselves and have been interpreted as cyanobacterial (Wright, 2000; Wright and Altermann, 2000).

Further support for a biogenic origin comes from the recent discovery of analogous pinnacle and cuspate growth forms in modern (perennially ice-covered) lacustrine environments in Antarctica (Andersen et al., 2011; Hawes et al., 2011; Sumner et al., 2015; 2016). These pinnacle and cuspate microbial mats are dominated by cyanobacteria of the *Leptolyngbya, Phormidium* and *Tychonema* genera and grow in environments with very low sedimentation rates (Andersen et al., 2011; Sumner et al., 2016). In modern environments the cuspate, pinnacle and conical morphologies observed are not solely related to light limitation, but reflect a combination of environmental factors, e.g. pH, salinity, sedimentation rate, biomass redistribution and accumulation, substrate topography, and microbial diversity and growth habit (Andersen et al., 2011; Shepard and Sumner, 2010; Sumner et al., 2016). The reticulate and cuspate structures developed by these mats form from the movement of motile, filamentous microbes, however, such structures can be produced by undirected gliding and collision of non-photosynthetic, filamentous microorganisms (Shepard and Sumner, 2010). Thus, the morphology of ancient cuspate stromatolites alone is not sufficient to infer the presence of cyanobacteria, but it can be strongly suggestive of a microbial (biogenic) origin (Bartley et al., 2014).

Observed textures show cyclicity (Figure 4) with support and drape structures likely forming under low energy conditions and contorted laminae forming in response to higher energy conditions (e.g., storm event) (Schröder et al., 2009). Alternatively, contorted laminae horizons may result from a chemical change in the paleoenvironment that led to death and deformation of the mat. As cuspate microbial mats grew at depths below wave-base (Sumner, 1997), it is unlikely that the contorted laminae formed as a result of desiccation, but changes in salinity, temperature or nutrient availability are all possible alternative explanations.

Hence, cuspate stromatolites from the Nauga Formation were selected for SRS-XRF scanning based on their unusual cuspate morphology and the relatively low-grade of alteration given their age. As such it should be possible to clearly map any observed spatial geochemical variation in their well preserved, and well-delineated, unusual stromatolitic structures.

3. Methods

3.1 Sample details, petrographic observations and XRD analysis

A 160 mm long, 45 mm wide, 6 mm thick slab from a cuspate stromatolite horizon within the Nauga Formation was sampled from core GKF01 (Schröder et al., 2006). Specific cuspate morphological elements/textures are identified as: support structures, drape structures, and contorted laminae (Figure 3). Abiotic textures are limited to lunate, void filling calcite cements (Figures 3 and 4). Petrographic analysis and XRD analysis were used to characterize both the mineralogy of the sample and the spatial

distribution of different carbonate phases with respect to microbial microtextures. Thin and polished sections were prepared at the University of Keele. Powders for XRD analysis and stained thin sections (alizarin red and potassium ferricyanide; Dickson, 1965) were prepared from six sites on the counterpart of the scanned cuspate stromatolite sample (Figure 4). Sites were selected that covered the variety of depositional fabrics visible within the sample. Analyses were conducted using a Bruker D8 Advance Diffractometer (Cu Kα X-Ray source) at the Williamson Research Centre (University of Manchester). Samples were scanned from 5 to 70° 2θ, using a step size of 0.02° and a counting time of 0.2 seconds per step; XRD spectra are shown in the supplementary information.

3.2 ICP-MS/AES analysis

ICP-MS/AES analysis was conducted to determine carbonate bound trace element and rare earth element and yttrium (REY) concentrations. These were used to assess the extent of detrital contamination and the likelihood of the preservation of a marine geochemical signal. ICP-MS and ICP-AES analyses were run at the Williamson Research Centre (University of Manchester) using an Agilent 7500cx Inductively Coupled Plasma Mass Spectrometer and a Perkin-Elmer Optima 5300 Dual View Inductively Coupled Plasma Atomic Emission Spectrometer respectively. Accuracy and precision were determined from known standards (at 1, 5, 10, 50, 100 ppb concentrations) with limits of detection typically 10-100 ppb on the ICP-AES and 0.01 to 0.1 ppb on the ICP-MS. A run of standards was performed after ten samples were analyzed. Each run of samples also contained four procedural blanks. REY accuracy was better than 3 % and relative standard deviation (RSD) lower than 6 %. Non-REY accuracy was better than 6 % and RSD lower than 6 %, with the exception of Al which at standard concentrations of 1 ppb had RSD values as high as 14 %. Samples were digested using previously published methods (Warke et al., 2018), further details are provided in the supplementary information. REY concentrations were normalized to Post Archean Australian Shale (PAAS; Taylor and McLennan, 1985) and are denoted as REY$_{SN}$. Anomalies of REY$_{SN}$ were calculated using the methods of Lawrence et al. (2006); details of these calculation methods are provided in the supplementary information.

3.3 SRS-XRF analysis and data processing

Synchrotron Rapid Scanning XRF (SRS-XRF) analysis was performed at the Stanford Synchrotron Radiation Lightsource (SSRL) using Beamline 6-2. The experimental protocol pertinent to this analysis is outlined here; more detailed information on the protocol and the data processing techniques and details regarding SRS-XRF theory and the SSRL facility are given elsewhere (Bergmann et al., 2010; 2012; Edwards et al., 2011; 2013; 2014; Wogelius et al., 2011).

The sample slab was mounted on a computer-controlled raster stage and lateral bidirectional scanning was then conducted using a predetermined x-y coordinate scan range, with a vertical step height of 80 µm and a fixed incident beam (50 µm diameter pinhole used in this experiment). Two scans were conducted using different incident X-Ray beam energies, to image the distribution of both High-Z and

Low-Z elements. High-Z scans were performed at 13.5 keV and optimized to resolve Ca, Pb, Mn, Fe, Cu, Zn, Ga, As, and Br. Low-Z scans were performed at 3.15 keV and optimized to resolve Al, Si, P, S, and Cl. Scans at 3.15 keV were conducted in a helium atmosphere to minimise beam attenuation and scattering of the fluorescence signal. Fluoresced X-Rays were detected with a 1 element Vortex silicon drift detector. Detection limits are typically ~1 ppm for heavier elements (13.5 keV scan) and between 1 and 100 ppm for lighter elements (3.15 keV scan; Bergmann et al., 2010; Edwards et al., 2013). An energy dispersive spectrum is not collected per pixel scanned but 16 channels (elements) are collected by setting windows on desired emission lines of the elements. These elements were chosen by performing a short scan over the sample's features of interest and surrounding areas to identify the dominant elements in the EDS spectra. Selection was done using several zones of interest to ensure elements are representative of the entire sample. Thus elements were chosen as a function of compositional information. The maps presented are 8 bit images generated from raw count data (i.e. min and max counts converted to 0 to 255 pixel intensity) and clipped at a range of percentiles (90, 95, 98, 99, 99.9, 99.99) using a custom MATLAB script. Hence, in the figures shown, each SRS-XRF map is scaled independently showing the relative differences in concentration in that element. Pixel brightness is not correlative between elemental maps.

To quantify the correlation between different elements, maps (98 % percentile) were compared using the ImageJ CorrelationJ plug-in (Abràmoff et al., 2004). Using the plug-in, regression analysis was performed on the pixel intensity of two element scans applying a local area size of 3 pixels; correlation coefficients for all elements scanned were generated, i.e. R and R^2 values (supplementary information: tables S2 and S3). Data scanned at 13.5 keV and 3.15 keV cannot be compared using the plug-in as they were scanned in separate experimental geometries and cannot not be precisely overlaid.

Point analyses (EDS spectra collected for 30 seconds at discrete locations) were collected to determine element concentrations at points of interest and calibrated to a Durango apatite (fluorapatite) mineral standard (Edwards et al., 2014). Locations of point analyses are shown in supplementary Figure S1. EDS spectra were fitted and quantified using PyMCA freeware (Solé et al., 2007). Peak fitting errors were calculated for each element and are given alongside determined concentrations in Table 3.

3.4 X-Ray Microtomography (XMT)

X-Ray Microtomography (XMT) was conducted to test whether the distinct morphologies (support and drape structures) characteristic of cuspate stromatolites could be imaged in 3D. Such images would improve comparison of ancient cuspate stromatolites with the morphology of modern pinnacle and cuspate mats. XMT was conducted at The Manchester X-Ray Imaging Facility at the University of Manchester using a Nikon customised bay with a 225 kV source (e.g. Streng et al., 2016). The sample was scanned twice; 3600 projections were collected from each scan. The first scan covered the entire sample and was conducted using an accelerating voltage of 115 kV, a current of 160 µA, a 0.5 mm copper filter, and was reconstructed to a 3D volume with a voxel size of 12 µm. The second scan was

conducted on a smaller region of interest using an accelerating voltage of 85 kV, a current of 175 µA, a 0.1 mm copper filter; the reconstructed 3D volume had a voxel size of 19 µm. Digital visualisation was achieved using open source volume renderer, Drishti (Limaye, 2012). Data (VGI and VOL files) were loaded into the programme using the Drishti importer and a range of transfer functions were applied to the 2D histogram to highlight features of interest. Images and movies were rendered and exported using Drishti.

4. Results

4.1 Petrographic observations and X-Ray Diffraction (XRD) results

Preserved cuspate (stromatolitic) structures (support, drape, and contorted laminae) consist of finely crystalline (~30 µm), planar-s to non-planar, ferroan dolospar (Figure 5A; Table 1). Within contorted laminae horizons and support structures, ferroan dolospar is sometimes spatially associated with small, equant, cubic, pyrite crystals (Figure 5B). Contorted laminae (Figure 5C) consist of thicker bands of ferroan dolomite (~200-400 µm) than drape structures (10-100 µm). At the top of contorted laminae layer 1 (Figure 4), contorted laminae are extensively fragmented and form isolated roll-ups and ovoid peloids (Figure 5D); peloids vary from ~80 µm up to 300 µm in diameter. Drape thickness is laterally variable; drapes are thickest where they are attached to support structures (typically ~100 µm; Figure 5E) and rapidly thin to tens of micrometers (Figure 5F). Drapes are sometimes observed to be continuous between supports, forming 'U-shaped' geometries (Figure 3; Figure 4).

Coarser (90-120 µm) grained, ferroan calcite is present between the ferroan dolomite mat structures and is the dominant carbonate phase within the sample (Figure 5). Finer (60-90 µm), equigranular, ferroan calcite also occurs within isolated pockets in contorted laminae and appears to infill porosity produced through mat roll-up (Figure 6A). Bladed ferroan calcite crystals are common in areas adjacent to mat structures; the long axes of these crystals are commonly perpendicular to the upward growth direction of support structures. These crystals show undular extinction that sweeps along the long axis of the ferroan calcite (Figure 6B). This property is characteristic of 'herringbone calcite' (Sumner and Grotzinger, 1996). Herringbone calcite nucleated on biogenic structures and is texturally distinct from the equigranular cements described above (Figure 6B). The centers of white, lunate cements consist of equigranular ferroan calcite, however the intensity of the staining is much less than is observed in the ferroan calcite precipitated between mat roll-up structures and peloids, suggesting a lower Fe content. Bulk rock XRD spectra (n=6) from three dolomite dominated sites and three calcite dominated sites show the presence of both calcite and dolomite (Table 1); dolomite ordering peaks are present (see SI for XRD spectra). Bulk rock XRD spectra from ferroan dolomite dominated sites on microbial structures (e.g. GAM 1A/3) do not show the presence of sulfides despite their detection using transmitted and reflected light microscopy.

Bulk rock XRD spectra also show the presence of quartz. Silica is most commonly present as microcrystalline silica spherules with diameters of ~500-800 μm, and radial growth and extinction patterns, which occur as isolated features or in small clusters (Figure 6C), but quartz cement is also present between ferroan calcite crystals in localized areas (Figure 6D). No silica veins (or veins of other compositions) are noted in association with the spherules and quartz precipitation. Small amplitude (up to 400 μm), bedding parallel, single stylolites (with limited bifurcation) are commonly seen within the contorted laminae layers and at the interface between dolomite and calcite dominated sections. They cross-cut sub-horizontal mat structures and are spatially associated with a high concentration of opaque minerals (Figure 6E and F).

4.2 ICP-MS/AES analysis

Element concentrations show bimodal variation between predominantly microbial fabrics (which are dolomite dominated) and non-microbial fabrics (calcite dominated). Concentrations of Fe, Mn and Mg are higher in microbial fabrics (supports, drapes, contorted laminae), as might be expected by the abundance of ferroan dolomite (Figure 5A; Table 1). In microbial fabrics Mg concentrations are up to 2.8 wt% and Mg/Ca ratios are ~0.09. Though Mg/Ca ratios are lower than expected for a dolomite, in these areas Fe/Ca ratios of ~0.2 (Fe: ~0.7 wt%) and Mn/Ca of ~0.3 (Mn: ~0.9 wt%) are noted. Areas drilled through microbial fabrics also incorporated some calcite from non-microbial fabrics, and so cation ratios (particularly Mg) from these samples will be lowered in the bulk rock results. In the non-microbial fabrics Mg/Ca and Fe/Ca ratios are much lower at 0.006-0.03 and 0.04-0.08 respectively, although Mn/Ca ratios (~0.2) are similar to the calcite-dominated microbial fabric. Strontium concentrations vary from 23-30 ppm and show no systematic variation with texture.

Dolomite-dominated microbial fabrics possess higher ΣREE concentrations. Ratios of Y/Ho (57-59) are lower in than in calcite-dominated non-microbial fabrics (67-75), but in both cases the Y/Ho are superchondritic (>44) (Figure 7). Cross-plots of ΣREE concentration against Al, Ti and Th show positive correlations (Figure S2).

4.3 SRS-XRF geochemical mapping and point analysis

Elemental distributions of Ca, Pb, Mn, Fe, Cu, Zn, Ga, As, and Br, are shown alongside the depositional fabric of the sample in Figure 8 where brighter pixels indicate a higher concentration. The distribution of Mn, Fe, and Ni is closely associated with dolomitized support, drape, and contorted laminae structures. Lunate cements show two zones of internal variation with respect to Mn (Figure 8). Copper is present within the contorted laminae and supports, and is less evident within drapes, with only one or two drapes showing a very low relative Cu content; As, Pb, and Br show a very similar distribution to Cu. Both Zn and Ga are homogeneously distributed across all fabrics, and show no strong correlation with support, drape, contorted laminae and lunate cements. Gallium shows some very low enrichment in the three contorted laminae bands. Relative calcium concentration shows an inverse distribution to

Mn, Fe and Ni being relatively lower within dolomitic stromatolite structures and higher in the surrounding fabric of the sample. The strongest spatial correlations exist between Mn and Fe (R = 0.95) and between Mn, Fe, and Ni (R > 0.7; tabulated R and R^2 values are in Supplementary Information).

Of the lighter elements (i.e. Al, Si, P, S, Cl; Figure 9), Al, Si, and P all correspond with stromatolitic textures. Silicon is concentrated along drapes. Sulphur shows relatively high concentrations within contorted laminae, supports and drapes. Chlorine shows weak association with the support, but it is largely homogeneously distributed across all fabrics. Like Mn, Cl is relatively concentrated along the outer margin of some lunate cements. A large area of relatively high Cl concentration does not correspond to a specific textural feature and is interpreted as an artefact possibly generated by accidental handling of the sample. Positive spatial correlations, where R > 0.65, are noted between Si, Al, and P (see supplementary information).

The SRS-XRF geochemical maps reveal additional textural features that are difficult to identify visually. Numerous small (<1 mm) spherical, rounded features can be seen concentrated along specific horizons in the Si, Al, P, and As maps. Two irregular, sub-linear features ('1' in Figure 8 and Figure 9) are strongly visible in the As, Al, Si, and P maps and weakly discernable in the Ga and S maps. One of these features is sub-horizontal, positioned at the top of contorted laminae layer 1, whereas the other is inclined at ~30 ° and crosscuts biogenic (mat laminae) structures.

Heavy element concentrations (and errors) for six point analyses are shown in Table 3, determined from specific points of interest (Figure S1) under an incident beam energy of 13.5 keV. The analyses show bimodality with respect to Ca, Mn, Fe, and As. Four points, located on clearly delineated stromatolitic textures, possess relatively lower Ca contents (21.8-27.7 wt%), and relatively higher Mn (3.1-4.3 wt%), Fe (3.5-5.3 wt%), As (9-87 ppm), and Cu (up to 20 ppm) concentrations. Two points on less developed stromatolitic textures have relatively higher Ca contents (~50.7 wt%) and Mn (1.2-1.4 wt%) and Fe (3184 and 3217 ppm) concentrations an order of magnitude lower than in the low Ca point analyses. High Ca points show much lower As (3-6 ppm) concentrations with Cu and Ga concentrations below the detection limit. Concentrations of Ga are uniformly low (< 3 ppm) and should thus be treated with caution given the minimum error is 1 ppm. Zinc concentrations do not show convincing bimodality, and range from 61-108 ppm.

Light element concentrations (Si, S, P, and Cl) were determined from five point analyses (Table 3). Silicon concentrations are higher than that of the other light elements and range from 1338 to 8188 ppm. Sulfur and phosphorous concentrations vary from 268 to 506 ppm and 240 to 431 ppm respectively; chlorine concentrations range from 321 to 733 ppm.

4.4 XMT imaging

Spherules are present throughout the sample (Figure 10), and their positions correspond to that observed in thin section and in several SRS-XRF maps. Some spherules are connected to lower density, linear structures which extend (and thin) upwards from the spherules in sub-vertical orientation, approximately orthogonal to bedding orientation (Figure 10). More commonly these structures are unconnected to spherules and also thin upwards (Figure 10); at least fourteen of these structures are identified. They occur in similar orientations and appear to terminate against an irregular, curved surface which possesses the concave-upward geometry commonly displayed by drapes. However, thin section observations also show a low amplitude stylolite present at that position which has a V-shaped geometry that mimics the geometry of closely associated drapes.

Surface scans (2D) of the lower portion of the sample are capable of visually distinguishing biogenic structures (dolomite) from the surrounding ferroan calcite. However, the biogenic structure is not well reproduced in 3D scans. This may be due to complications conferred by the dimensions of the sample, particularly its thickness (6 mm) relative to the 2D surface area scanned (45 x 60 mm) but could also result from a lack of X-Ray attenuation contrast between the phases of interest. In the lower portions of the sample spherules are present, but the sub-vertical structures are mostly absent. Lunate cements and discontinuous supports can also be seen; sub-linear and sub-vertical structures near the base of the sample correspond to areas of void space on the surface of the sample (Figure S3). A dense, horizontal band corresponds to the position of a prominent, bifurcating stylolite described above (Figure 6F).

5. Discussion

5.1 Element distribution within cuspate microbial textures

5.1.1. Origin of metals in stromatolite structures

Several elements (Ca, Fe, Mn, Ni, Cu, As, Br, Al, Si, P, S, Cl) mapped using SRS-XRF show a strong spatial correlation with preserved cuspate stromatolitic textures over decimeter scales (Figures 8; 9). This significant visual contrast between stromatolitic (biogenic support, drape and contorted laminae structures) and non-stromatolitic (abiogenic cements) textures corresponds directly to differences in the predominant carbonate mineralogy. Therefore it is highly probable that this bimodality in dominant carbonate mineral distribution is the principal control on the quantified differences in element distribution. This suggests a mineralogical control over element incorporation into the respective crystal structures.

The partition coefficient (K_D) controls the relative distribution of metal ions between pore fluids and carbonate minerals (Veizer, 1983). Minerals can incorporate metal ions such as Zn^{2+}, Fe^{2+}, Cu^{2+}, in place of Ca^{2+} or Mg^{2+} in the carbonate lattice, while non-metals like As^{3+} can be incorporated as arsenate in place of the carbonate complex (Winkel et al., 2013; Petrash et al., 2015; Sforna et al., 2017).

However, cations with an ionic radius smaller than Ca (0.99 Å) are preferentially incorporated into dolomite, i.e. many of the trace elements relevant here have higher partition coefficients for dolomite than calcite (e.g. Fe, Mn, Cu, Ni; Kretz, 1982; Veizer, 1983; Morse and Bender, 1990). This is consistent with the observed enrichment factors in dolomite relative to calcite; in dolomite Fe is 2.2-4.3 times higher using ICP-MS and 11-16 times higher using SRS-XRF and Mn is 1.2-1.4 times higher in dolomite using ICP-MS and 2.3-3.5 times higher using SRS-XRF.

Therefore, although element distributions correlate strongly with stromatolitic textures, it seems likely that element distributions are principally controlled by the spatial limitation of dolomite to supports, drapes, and contorted laminae. The same spatial restriction of dolomite opens the possibility that microbial processes may have been responsible for dolomite precipitation, and ultimately for element distributions. Addressing this hypothesis depends on identification of probable dolomitization pathways. Possible mechanisms and timing of dolomitization are discussed below (section 5.3). It should further be noted that calcite and dolomite quite possibly formed from different fluids of potentially very different trace element composition and under variable physicochemical conditions, which would contribute to the difference in observed trace element concentrations

Despite these uncertainties observed trace metal concentrations can be used to assess potential pore fluids from which metals precipitated (see Supplementary Information; Tables S1-S3). This rests on numerous assumptions, as experimental K_D values show large variability due to experimental conditions, dependence on precipitation rate and temperature, as well as possible biological effects (Dromgoole and Walter, 1990; Morse and Bender, 1990). Potential fluid types relevant to this study are Archean seawater (for marine calcite precipitation and dolomitization) and basinal brines (in the case of burial dolomitization). Limited compositional data is available for the former, whereas fluids from the modern crust approximate brines (Table S5). Modern seawater, which is well constrained, is used as a reference; it might also approximate trace metal concentrations in Archean meteoric waters.

The analysis (see Supplementary Information) shows that the high measured concentrations of Fe, and Mn require pore water concentrations of approximately 1 ppm or more, i.e. 1000-10000 times modern seawater concentrations (e.g. Veizer, 1983; Danielsson, 1980). Measured concentrations are instead compatible with Archean seawater (Table S6). Iron concentrations of 1 ppm would inhibit calcite precipitation (Dromgoole and Walter, 1990; Sumner, 1997), while concentrations of 43 ppm are required for banded iron formations (Ewers, 1983; Sumner, 1997). It is estimated that Archean anoxic seawater in equilibrium with rhodochrosite could have supported Mn concentrations of about 5 ppm (Crerar et al., 1980; Anbar and Knoll, 2002). Due to their reducing nature, basinal brines, interacting with carbonate sediments during burial diagenesis, are another potential cation source. Cation concentrations vary strongly in these fluids (Sverjensky, 1987). Measured concentrations of Mn and Fe in calcite are compatible with brines of lower Fe concentrations (few ppm to few 10's ppm) and all published Mn concentrations (Table S6). On the other hand, the measured concentrations of Cu and Zn are 1-2 orders of magnitude smaller than those expected from basinal brines (Table S6). Experimental distribution

coefficients tend to be highest at the low precipitation rates and high temperatures of brines, so trace element concentrations at the high end of those reported in Table S6 should be expected. On that basis, brines are a potential fluid source for Fe and Mn, but unlikely to have produced the observed Cu and Zn concentrations. Archean seawater is more compatible with all observations

5.1.2 Si, Al, and detrital impact

Silica and aluminum are relatively enriched within support structures and drapes likely reflecting either: (i) incorporation of allogenic, fine-grade, detrital material, or (ii) authigenic silica precipitation (biotic or abiotic) within the mat. Though some minor silicification is seen elsewhere (e.g. in tension gashes, spherules) that may be attributable to later fluids, this manner of silicification does not spatially coincide with silica distribution in, and microfacies observations of, supports and drapes.

No detrital grains (silt or fine-sand grade) were identified in thin section. Previous petrographic studies also failed to identify fine-grained detrital material, and inferred that detrital input into the distal environment where cuspate microbial mats were growing was negligible (Sumner, 1997). In modern environments delicate cuspate morphologies are only preserved in environments with very low detrital input (Andersen et al., 2011; Sumner et al., 2016). However, while both calcite and dolomite dominated portions of the sample preserve marine REY_{SN} characteristics (discussed below), there is correlation between ΣREE and detrital indicators (Figure S2). This suggests that there may have been some very fine-grained detrital input into the mat, possibly clays that were trapped by adhesive extracellular polymeric substances (EPS). Clays were deposited in nearby environments, as implied the observation that Nauga carbonates are interbedded with shales (Schröder et al., 2009).

Alternatively, Si distribution may be attributable to authigenic processes. For example, bacterial binding of Fe and Al can promote authigenic silica precipitation, which could explain the spatial association of Si with Al (R >0.65). However, non-bacterially mediated processes dominate in solutions with a high iron concentration, such as Neoarchean sea/pore water (Fein et al., 2002; Phoenix et al., 2003; Eroglu et al., 2018). Abiogenic silica precipitation could have been facilitated by the higher amounts of dissolved silica in Neoarchean seawater (1.25-1.45 mM) which are approximately 20 times greater than the modern ocean (Maliva et al., 1989; 2005; Siever, 1992). However, in most cases the silicification of Archean and Proterozoic carbonates is limited to peritidal environments with a high rate of evaporation (Maliva et al., 2005; Manning-Berg and Kah, 2017), but not subtidal, platform-slope environments such as those preserved by the Nauga Formation. Also, in these instances silicification (typically expressed as replacive, early diagenetic chert) is pervasive and easily recognized in thin section. In contrast, the Si distribution noted in this sample is cryptically preserved and cannot be observed easily in thin section.

Therefore, a detrital origin for the observed Si and Al distributions is most consistent with the current evidence, although authigenic origin cannot be ruled out. In either case, recognizing the close spatial

association of Si and Al with dolomitized microbial elements has only proved possible with use of SRS-XRF, highlighting the utility of the technique in deciphering subtle geochemical variations.

5.2 Element distribution within non-stromatolitic textures

No difference in the relative Ca or Fe concentration is seen between bladed herringbone calcite textures and equigranular, ferroan calcite in the SRS-XRF maps. In thin section equigranular calcite precipitated between rolled up mat elements in contorted laminae layers carries a stronger alizarin red and potassium ferricyanide staining than equigranular calcite the center of lunate cements. This suggests differences in iron concentration. Equigranular ferroan calcite is interpreted as having infilled primary porosity between mat elements. Herringbone calcite textures within the Gamohaan Formation have been interpreted as syndepositional growth forms which crystallized directly from seawater and were nucleated on supports and drapes (Sumner and Grotzinger, 1996; Sumner, 1997).

The precipitation of equigranular ferroan calcite in lunate cements postdates the precipitation of herringbone fabrics (Figure 6B). However, precipitation of this phase likely occurred prior to significant burial of the mat as early cementation would have been necessary to protect the intricate cuspate morphology from being crushed and obliterated during compaction. It is possible that a previous cement phase was present and was subsequently replaced by that which is currently preserved, but there is no clear petrographic evidence and it is noted that lunate cements still preserve marine REY_{SN} patterns and anomalies. However, ring-shaped enrichments in Cl and Mn on the outer margins of lunate cements (Figure 7; 9) could suggest that primary porosity was occluded by at least two fluids, and that either the composition of the cement forming fluid changed over time and/or there was some recrystallization flowing later diagenetic fluid flow. While further work is needed to fully understand these geochemical variations, their identification has only proved possible using SRS-XRF underlining the applicability of this technique to paragenetic studies.

The sub-horizontal, irregular, linear features that are prominent within the As, Al, Si, and P maps also correspond to the position of isolated, small amplitude stylolites in thin section (Figure 6E and F) and the high density feature imaged using XMT (Figure S2). The elevated elemental concentrations observed on stylolites reflect accumulation of insoluble residue during chemical compaction and dissolution.

5.3 Principal controls on element distribution

This pathfinder study has shown that SRS-XRF can detect heterogeneous trace element distribution within an ancient stromatolite on a decimeter scale. The following section discusses whether any observed variations could to be tied to the composition of Neoarchean seawater or mat-water, or whether trace element distributions could suggest the presence of particular microorganisms via the products of their metabolic pathways, particularly cyanobacterial photosynthesis.

5.3.1 Dolomitization

As the distribution of most elements is spatially linked to the distribution of ferroan dolomite, the timing and mechanisms of dolomite formation need to be understood. Early petrographic work on the cuspate stromatolites of the Gamohaan Formation noted the occurrence of fine grained, non-planar ferroan dolospar as well as organic inclusions within biogenic structures that are encased by syndepositional herringbone calcite (Sumner 1997; Sumner and Grotzinger, 1996). However, probable dolomitization pathways were not proposed (Sumner 1997; 2000). Possible dolomitization mechanisms include burial fluids, microbial sulfate reduction (MSR), mat degradation, and seawater dolomitization. Observations presented here can provide constraints on which mechanisms were most likely.

Extensive interaction of herringbone calcite textures with basin-derived dolomitizing brines during deep burial is noted elsewhere in the Gamohaan Formation where it results in recrystallization of herringbone calcite fabrics to equigranular fabrics (Sumner and Grotzinger, 1996); less extensive interaction can cause fabric-retentive dolomitization of herringbone fabrics (Sumner and Grotzinger, 1996). Such fluids could have migrated through fractures or along stylolites, which can act as fluid migration pathways (Heap et al., 2014). However, no veins are seen in this sample and there is no petrographic evidence for dolomitization along the length of dissolution structures. Contorted laminae, support and drape structures that are unassociated with stylolites have still undergone dolomitization but are surrounded and separated by ferroan calcite. Both calcite and dolomite dominated portions of the sample preserve REY_{SN} patterns that show heavy REE enrichment, positive Gd_{SN}, Eu_{SN} and La_{SN} anomalies and superchondritic Y/Ho ratios (>44) (Allwood et al., 2010). Overall, PAAS-normalised REY_{SN} patterns (Figure 7) and anomalies are consistent with Neoarchean seawater rather than burial brines (see also Kamber and Webb, 2001) which is further supported by the analysis of trace elements (Supplementary Information).These observations could suggest that dolomite formed in the early stages of burial, before all porosity was occluded by ferroan calcite cements - as has been previously argued (Wright, 2000; Wright and Altermann, 2000; Altermann et al., 2006) – and that the dolomitization may have been driven by near-surface fluids. Nevertheless, although a marine signal dominates, the low observed Sr concentrations suggest that some interaction with non-marine (meteoric or burial) fluids may have occurred during diagenesis (Banner, 1995).

Previous studies have proposed that dolomitization within the Gamohaan Formation was controlled by microbial sulfate reduction (MSR) within the microbial mat (Wright, 2000; Wright and Altermann, 2000). Sulfate-reducing microbes metabolize SO_4^{2-}, H^+, and Na^+, dissociating seawater $MgSO_4$ in the process (Baker and Kastner, 1981; Vasconcelos et al., 1995; Vasconcelos and McKenzie, 1997; Warthmann et al., 2000; van Lith et al., 2003a; 2003b). The presence of $MgSO_4$ constitutes a kinetic barrier to dolomite formation (Baker and Kastner, 1981) but its removal promotes dolomite precipitation by releasing Mg^{2+} ions through mat degradation and increasing pH and carbonate alkalinity (Vasconcelos et al., 1995; Vasconcelos and McKenzie, 1997; Warthmann et al., 2000; van Lith et al., 2003a; 2003b). Some have

argued this mechanism of dolomite formation may have been very significant prior to the GOE (Warthmann et al., 2000; Vasconcelos et al., 2006).

Sulfate was present in Neoarchean seawater, however, its low concentration (<200 μM, possibly as low as ~2.5 μM) is considered to have limited MSR (Habicht et al., 2002; Crowe et al., 2014; Zhelezinskaia et al., 2014). Fractionations in $\delta^{34}S$ that are consistent with MSR are noted in portions of the Gamohaan Formation (Kamber and Whitehouse, 2007), however these *in-situ* measurements were made on more abundant, spheroidal pyrite in calcite-dominated horizons, which were not observed in this study. Large fractionations in $\delta^{34}S$ do not require the existence of a large pool of seawater sulfate but can occur due to Rayleigh distillation effects in a limited sulfate pool (Meyer et al., 2016). Due to such low sulfate concentrations it is unlikely that sulfate pairing with Mg^{2+} ions in seawater constituted a significant kinetic barrier to dolomite formation as it does today (Baker and Kastner, 1981; Morrow and Ricketts, 1988). Dolomitization driven by MSR should also lead to pyrite formation throughout the cuspate structures, given the high levels of Fe^{2+} (60-928 μM) that were likely present in seawater and pore waters for reaction with hydrogen sulfide (Eroglu et al., 2018). While some cubic pyrite crystals are observed in cuspate structures (Figure 5B), overall the proportion of sulfides remains very low, such that none are detected in bulk rock XRD analysis (Table 1). Therefore, it is not possible to totally exclude MSR as having had an effect on dolomitization, but it is unlikely to be the dominant process as MSR was likely suppressed by low sulfate levels (Crowe et al., 2014).

Marine REY_{SN} patterns and the trace element compositions (analyzed in section 5.1.1) argue against a significant contribution from burial brines, which are a potential source of abundant Mg. Some Mg for dolomite nucleation may have been sourced locally from the degrading mat. It has been previously proposed that degradation of Mg^{2+} rich bacterial sheaths could have released Mg^{2+} ions for dolomite precipitation, particularly as cuspate stromatolites in the Gamohaan Formation are more pervasively dolomitized where (interpreted) bacterial sheaths are degraded (Wright, 2000; Wright and Altermann, 2000). Biofilms can control uptake of trace elements into the EPS, including kinetic inhibitors to carbonate precipitation (e.g. Mg; Bosak and Newman, 2005; Braissant et al., 2007; Dupraz et al., 2009). Cation release and biologically-influenced organomineralization can occur via: (i) increase of external cation concentrations (e.g. via changes in pore-water salinity and alkalinity), thereby saturating the cation binding capacity of EPS; (ii) hydrolysis of EPS; (iii) acidic EPS templates for precipitation (Decho, 2000; Dupraz et al., 2009; Bontognali et al., 2010). This process has been related to dolomite formation in supratidal mats of the Abu Dhabi sabkha (Bontognali et al., 2010). Additionally, organic acids generated during the degradation of organic matter in the mat may have chelated Mg^{2+} from detrital silicates (Wogelius and Walther, 1991). As discussed earlier, some fine-grained detrital input may be suggested by the distribution of Si and Al (Figure 9). If dolomitization was initiated by mat-intrinsic Mg^{2+}, it might explain why only the cuspate structures became dolomitized and the (interpreted) syndepositional ferroan calcite phases were not.

Seawater circulation provides the most abundant and continuous source of Mg (Land, 1985). Dolomite-dominated portions of the sample record marine REY_{SN} patterns, anomalies, and trace element fractionations suggesting a seawater-derived dolomitizing fluid was derived from seawater. Neoarchean seawater was reduced and accordingly contained high amounts of reduced metals such as Fe^{2+}, Mn^{2+} and Mg^{2+} which were sourced from hydrothermal/volcanic inputs into seawater (Klein, 2005). Ferrous iron and manganese would have been readily incorporated into the carbonate lattice in cation sites during the initial precipitation of calcite (see trace element discussion, Supplementary Information). Circulation and infiltration of Mg^{2+} rich seawater-derived fluids of seawater through the platform margin and slope, possibly during sea-level falls, may have caused dolomitization. Porosity may then have been closed by later precipitation of ferroan calcite cements; these also would likely have precipitated from a seawater derived fluid given that they also preserve marine REY_{SN} characteristics, including superchondritic Y/Ho fractionation and positive Eu_{SN} anomalies (Eroglu et al., 2018).

5.3.2 Biofilms and trace metal accumulation

The spatial association of dolomite with biogenic structures, and the trace element enrichment in dolomite, can therefore reflect the combined effects of a biofilm and seawater dolomitization. This allows the possibility that microbial communities influenced trace element accumulation, which would provide a biosignature.

Cyanobacteria exert a high demand for Cu, Mn, Fe, As, and Ni, given the importance of these elements in key biological processes, most notably their role as cofactors in oxygenic photosynthesis (Raven, 1999; Shcolnick and Keren, 2006; Huertas et al., 2014; Sforna et al., 2014). For instance, Cu is incorporated into the cyanobacterial thylakoid to produce the protein plastocyanin that is key to the operation of photosystem II, as also is Mn (Huertas et al., 2014; Shcolnick and Keren, 2006). However, in order to be tied to a specific metabolic pathway, trace metals must have undergone bioaccumulation; this is distinct from passive binding of metal cations by EPS (Sforna et al., 2017). To identify this distinction previous synchrotron-based studies of ancient and modern stromatolites were, by necessity, highly spatially focused and have been conducted at a µm to (maximum) cm scale (e.g. Lepot et al., 2008; 2009; Sforna et al., 2014; 2017). These studies have elucidated important aspects of trace metal distribution in ancient microbialites, including differentiation between whether these can be attributed to bioaccumulation rather than passive binding processes through examination of µm-scale structures.

In the SRS-XRF maps obtained several trace elements (Ni, Cu, As, Br, Al, Si, P, S) and major elements (Ca, Fe, Mn) that map closely to biogenic structures from which filamentous microfossils have been reported. However, as discussed above, both the distribution and concentration of these elements are strongly controlled by the dominant carbonate mineralogy, and therefore dolomitization. While it remains possible that microbial communities at least influenced the trace element distribution in

dolomite, the present-day distribution is more likely a result of buffering by pore water combined with diagenetic recrystallization.

Biofilms tend to be porous, allowing fluid flow through the mat. As discussed above, uptake of trace elements into the EPS, followed by cation release in response to changes in pore water salinity or alkalinity (Decho, 2000), provide a mechanism for microbially-influenced nucleation of dolomite seed crystals, thereby explaining the spatial association of dolomite and biogenic structures in the studied sample. Biologically-influenced organomineralization onto EPS templates would have been particularly effective under conditions of low Ca concentration and elevated dissolved inorganic carbon (DIC), such as postulated for much of the Precambrian (Grotzinger and Knoll, 1999; Arp et al., 2001; Bosak and Newman, 2005).

However, in modern settings such dolomite organominerals only make up a small fraction of the sediment (~5 vol.%; Machel, 2004), so they are unlikely the main cause of platform dolomitization as in the Campbellrand. While they could provide seed crystals, the continued growth of these minerals, and their bulk trace element budget were more likely controlled by thermodynamic exchange with the pore fluid. The medium would be buffered by the high DIC (Bosak and Newman, 2005). Precipitation in low Ca/high DIC alkaline lakes is essentially physicochemically driven, even when using EPS templates (Arp et al., 2001). Experimental work has demonstrated that thermodynamic precipitation dominates at low Ca concentrations (Dickinson et al., 2002). Although organometallic complexes formed in the EPS can be transferred into carbonate minerals, overall crystal growth and chemistry tend to be dominated by the pore fluid (Petrash et al., 2015; Sforna et al., 2017).

5.4 Future application of SRS-XRF in microbialite studies

Setting the limitations of this sample aside, it has been shown that quantitative, dm-scale elemental maps can be obtained from ancient microbialites using SRS-XRF; this contribution reflects the first time this technique has been used for such samples. As noted above, previous synchrotron studies have been conducted at much smaller scales, however SRS-XRF offers unique advantages over a more spatially focused approach. Designed to operate at dm scales, SRS-XRF is a more appropriate, faster, and non-destructive technique for fully characterizing the trace metal distribution across an entire sample at ~20-100 μm resolution, whilst maintaining ppm sensitivity; this cannot be achieved with more conventional synchrotron or laboratory-based techniques. As such, it can allow a better determination of whether or not an area chosen for analysis at a higher resolution is truly representative of the sample as a whole and be used to guide further analyses. SRS-XRF is the only method capable of determining quantifiable, trace element distributions at the decimeter scale – i.e. one to two orders of magnitude greater than can be achieved with other techniques – and that is also nondestructive, whilst maintaining both resolution and sensitivity.

SRS-XRF may have several applications in the field of microbialite research. For example, as demonstrated by this contribution, when coupled with other petrographic methods, decimeter scale SRS-XRF element maps are valuable in deciphering a sample's paragenetic evolution by allowing interrogation of large, widely spaced structures (e.g. stylolites, tension gashes, veins, concretions, microbial textures) on cm and dm scales. Such structures may be missed in higher resolution studies.

SRS-XRF scans can also reveal important areas of interest – "hotspots" (Sforna et al., 2017) – for further, higher resolution analysis, such as those approaches taken for distinguishing between bioaccumulated or passively bound trace metals. As such SRS-XRF may represent a way of initially interpreting a specimen prior to conducting a more spatially focused and/or destructive technique. SRS-XRF could be used to map trace element distribution in living (or recently deceased) microbial mats as this has not yet been conducted on a decimeter scale. Further investigation of non-dolomitized microbialites could also be conducted to look for evidence of bioaccumulated or passively bound trace metals in stromatolites. It is also possible that SRS-XRF could also be applied in microfossil investigations.

6. Conclusions

This pathfinder study shows that heterogeneous element distributions can be quantified and mapped in Neoarchean stromatolites at high resolution/sensitivity but on a decimeter scale. Cuspate stromatolite structures contain relatively higher proportions of Fe, Mn, Pb, Cu, As, Br, Al, Si, P, and S. Integration of SRS-XRF geochemical mapping with petrographic imaging suggests that trace element distribution within the Upper Nauga Formation cuspate stromatolites is controlled by the carbonate mineralogy. Interpreted biogenic structures solely consist of ferroan dolomite which preferentially partitions small diameter cations such as Mn, Fe, Ni and Cu from the dolomitizing fluid into the dolomite lattice. Dolomitization occurred either syndepositionally or during shallow burial. The spatial association of dolomite to microbial structures could relate to microbially-influenced dolomite nucleation, but dolomitization was driven by Neoarchean seawater-derived fluids, not basin-derived brines. Therefore, the dolomitized cuspate stromatolites can still record information about seawater composition, in addition to information about early diagenesis and dolomitization during the Neoarchean.

SRS-XRF compliments the existing suite of synchrotron techniques applied to the investigation of ancient stromatolites, adding the ability to produce large scale maps of trace metal distributions at spatially high resolutions (up to ~20 μm) at ppm sensitivity. It may be a useful first analysis in any such investigation; used to fully characterize the sample, observe any diagenetic features that may have altered the sample's geochemical make-up, and identify specific areas of interest, allowing for better targeting of high-resolution studies. Therefore, SRS-XRF, coupled with X-Ray absorption spectroscopy to help diagnose coordination chemistry of elements, will prove important tools for geochemical analysis of ancient microbialites and could be used to help resolve fundamental questions in geomicrobiology

and stromatolite petrography, including: diagenesis, trace metal availability/usage, biogenicity, and constraining the emergence of particular microorganisms and metabolic processes.

7. Acknowledgements

8. References

Abràmoff, M.D., Magalhães, P.J. and Ram, S.J. (2004) Image processing with ImageJ. *Biophotonics international*, **11**, 36-42.

Allwood, A.C., Kamber, B.S., Walter, M.R., Burch, I.W. and Kanik, I. (2010) Trace elements record depositional history of an Early Archean stromatolitic carbonate platform. *Chem. Geol.* **270,** 148-163.

Altermann, W. and Nelson, D.R. (1998) Sedimentation rates, basin analysis and regional correlations of three Neoarchaean and Palaeoproterozoic sub-basins of the Kaapvaal craton as inferred from precise U–Pb zircon ages from volcaniclastic sediments. *Sediment. Geol.*, **120**, 225-256.

Altermann, W., Kazmierczak, J., Oren, A. and Wright, D.T. (2006) Cyanobacterial calcification and its rock-building potential during 3.5 billion years of Earth history. *Geobiology*, **4**, 147-166.

Anbar, A.D. and Holland, H.D. (1992) The photochemistry of manganese and the origin of banded iron formations. *Geochim. Cosmochim. Acta*, **56**, 2595-2603.

Anbar, A.D. and Knoll, A.H. (2002) Proterozoic ocean chemistry and evolution: a bioinorganic bridge? *Science*, **297**, 1137-1142.

Andersen, D.T., Sumner, D.Y., Hawes, I., Webster-Brown, J. and McKay, C.P. (2011) Discovery of large conical stromatolites in Lake Untersee, Antarctica. *Geobiology*, **9**, 280-293.

Arp, G., Reimer, A. and Reitner, J. (2001) Photosynthesis-induced biofilm calcification and calcium concentrations in Phanerozoic oceans. *Science,* **292**, 1701-1704.

Baker, P.A. and Kastner, M. (1981) Constraints on the formation of sedimentary dolomite. *Science*, **213**, 214-216.

Bartley, J.K., Kah, L.C., Frank, T.D. and Lyons, T.W., (2014) Deep-water microbialites of the Mesoproterozoic Dismal Lakes Group: microbial growth, lithification, and implications for coniform stromatolites. *Geobiology*, **13**, 15-32.

Bekker, A., Holland, H.D., Wang, P-L, Rumble III, D., Stein, H.J., Hannah, J.L., Coetzee, L.L. and Beukes, N.J. (2004) Dating the rise of atmospheric oxygen. *Nature*, **427**, 117-120.

Bergmann, U., Morton, R.W., Manning, P.L., Sellers, W.I., Farrar, S., Huntley, K.G., Wogelius, R.A. and Larson, P. (2010) *Archaeopteryx* feathers and bone chemistry fully revealed via synchrotron imaging. *Proc. Natl Acad Sci. USA*, **107**, 9060-9065.

Bergmann, U., Manning, P.L. and Wogelius, R.A. (2012) Chemical mapping of paleontological and archeological artifacts with synchrotron X-rays. *An. Rev. Anal. Chem.*, **5**, 361-389.

Beukes, N.J. (1987) Facies relations, depositional environments and diagenesis in a major early Proterozoic stromatolitic carbonate platform to basinal sequence, Campbellrand Subgroup, Transvaal Supergroup, Southern Africa. *Sediment. Geol.*, **54**, 1-46.

Bontognali, T.R., Vasconcelos, C., Warthmann, R., Bernasconi, S.M., Dupraz, C., Strohmenger, C.J. and McKenzie, J.A. (2010) Dolomite formation within microbial mats in the coastal sabkha of Abu Dhabi (United Arab Emirates). *Sedimentology,* **57**, 824-844.

Bosak, T. and Newman, D.K. (2005) Microbial kinetic controls on calcite morphology in supersaturated solutions. *Journal of Sedimentary Research*, **75**, 190-199.

Bowring, S.A. and Ross, G.M. (1985) Geochronology of the Narakay Volcanic Complex: implications for the age of the Coppermine Homocline and Mackenzie igneous events. *Can. Journ. of Earth Sci.*, **22**, 774-781.

Braissant, O., Decho, A.W., Dupraz, C., Glunk, C., Przekop, K.M. and Visscher, P.T. (2007) Exopolymeric substances of sulfate-reducing bacteria: Interactions with calcium at alkaline pH and implication for formation of carbonate minerals. *Geobiology*, **5**, 401-411.

Brasier, M.D., Green, O.R., Jephcoat, A.P., Kleppe, A.K., Van Kranendonk, M.J., Lindsay, J.F., Steele, A. and Grassineau, N.V. (2002) Questioning the evidence for Earth's oldest fossils. *Nature*, **416**, 76-81.

Brasier, M.D., Green, O.R., Lindsay, J.F., McLoughlin, N., Steele, A. and Stoakes, C. (2005) Critical testing of Earth's oldest putative fossil assemblage from the~ 3.5 Ga Apex chert, Chinaman Creek, Western Australia. *Precambr. Res.*, **140**, 55-102.

Brocks, J.J., Logan, G.A., Buick, R. and Summons, R.E. (1999) Archean molecular fossils and the early rise of eukaryotes. *Science*, **285**, 1033-1036.

Butterfield, N.J. (2015). Proterozoic photosynthesis–A critical review. *Palaeontology*, **58**, 953-972.

Canfield, D.E. (2005) The early history of atmospheric oxygen: homage to Robert M. Garrels. *Annual Rev. Earth Planet. Sci.*, **33,** 1-36.

Crerar, D.A., Fischer, A.G. and Plaza, C.L. (1980) Metallogenium and biogenic deposition of manganese from Precambrian to recent time, in: Varentsov, I.M., Grasselly, G. (Eds.), Geology and geochemistry of manganese. Akademiai Kiado, 285-304.

Crowe, S.A., Paris, G., Katsev, S., Jones, C., Kim, S.T., Zerkle, A.L., Nomosatryo, S., Fowle, D.A., Adkins, J.F., Sessions, A.L. and Farquhar, J. (2014) Sulfate was a trace constituent of Archean seawater. *Science*, **346**, 735-739.

Czaja, A.D., Beukes, N.J. and Osterhout, J.T. (2016) Sulfur-oxidizing bacteria prior to the Great Oxidation Event from the 2.52 Ga Gamohaan Formation of South Africa. *Geology*, **44**, 983-986.

Danielsson, L.G. (1980) Cadmium, cobalt, copper, iron, lead, nickel and zinc in Indian-Ocean water *Mar. Chem.*, **8**, 199-215

De Ronde, C.E., deR Channer, D.M., Faure, K., Bray, C.J. and Spooner, E.T. (1997) Fluid chemistry of Archean seafloor hydrothermal vents: Implications for the composition of circa 3.2 Ga seawater. *Geochim. Cosmochim. Acta*, **61**, 4025-4042.

Decho, A.W. (2000) Exopolymer-mediated microdomains as a structuring agent for microbial activities. In: Riding, R. and Awramik, S.M. (Eds) Microbial Sediments. Springer-Verlag, Berlin, 9–15.

Dickson, J.A.D. (1965) A modified staining technique for carbonates in thin section. *Nature*, **205**, 587.

Dickinson, S.R., Henderson, G.E. and McGrath, K.M. (2002) Controlling the kinetic versus thermodynamic crystallisation of calcium carbonate. *Journal of Crystal Growth*, **244**, 369-378.

Dromgoole, E.L. and Walter, L.M. (1990) Iron and manganese incorporation into calcite: Effects of growth kinetics, temperature and solution chemistry. *Chem. Geol.*, **81**, 311-336.

Dupraz, C., Reid, R.P., Braissant, O., Decho, A.W., Norman, R.S. and Visscher, P.T. (2009) Processes of carbonate precipitation in modern microbial mats. *Earth-Sci. Rev.*, **96**, 141-162.

Edwards, N.P., Barden, H.E., van Dongen, B.E., Manning, P.L., Larson, P.L., Bergmann, U., Sellers, W.I. and Wogelius, R.A. (2011) Infrared mapping resolves soft tissue preservation in 50 million year-old reptile skin. *Proc. Royal Soc. London B: Bio. Sci.*, **278**, 3209-3218.

Edwards, N.P., Wogelius, R.A., Bergmann, U., Larson, P., Sellers, W.I. and Manning, P.L. (2013) Mapping prehistoric ghosts in the synchrotron. *Applied Physics A*, **111**, 147-155.

Edwards, N.P., Manning, P.L., Bergmann, U., Larson, P., van Dongen, B.E., Sellers, W.I., Webb, S.M., Sokaras, D., Alonso-Mori, R., Igantyev, K., Barden, H.E., van Veelen, A., Anné, J., Egerton, V.M. and Wogelius, R.A. (2014) Leaf metallome preserved over 50 million years. *Metallomics*, **6**, 774-782.

Eroglu, S., Schoenberg, R., Pascarelli, S., Beukes, N.J., Kleinhanns, I.C. and Swanner, E.D., 2018. Open ocean vs. continentally-derived iron cycles along the Neoarchean Campbellrand-Malmani Carbonate platform, South Africa. *Am. J. Sci.*, **318**, 367-408.

Ewers, W.E. (1983) Chemical factors in the deposition and diagenesis of banded iron formation, in: Trendall, A.F., Morris, R.C. (Eds.), Iron-formation: Facts and problems. Elsevier, Amsterdam, 491-512.

Farquhar, J., Bao, H. and Thiemens, M. (2000) Atmospheric Influence of Earth's Earliest Sulfur Cycle. *Science*, **289**, 756-758.

Farquhar, J., Zerkle, A.L. and Bekker, A. (2011) Geological constraints on the origin of oxygenic photosynthesis. *Photosynthesis Research*, **107**, 11-36.

Fein, J. B., Scott, S. and Rivera, N. (2002) The effect of Fe on Si adsorption by Bacillus subtilis cell walls: insights into non-Ferometabolic bacterial precipitation of silicate minerals. *Chem. Geol.* **182**, 265-273.

Fischer, W.W., Hemp, J. and Johnson, J.E. (2016) Evolution of oxygenic photosynthesis. *Annual Rev. Earth Planet. Sci.*, **44**, 647-683.

French, K.L., Hallmann, C., Hope, J.M., Schoon, P.L., Zumberge, J.A., Hoshino, Y., Peters, C.A., George, S.C., Love, G.D., Brocks, J.J. and Buick, R. (2015) Reappraisal of hydrocarbon biomarkers in Archean rocks. *Proc. Natl Acad Sci. USA*, **112**, 5915-5920.

Garvin, J., Buick, R., Anbar, A.D., Arnold, G.L. and Kaufman, A.J. (2009) Isotopic Evidence for an Aerobic Nitrogen Cycle in the Latest Archean. *Science*, **323**, 1045-1047.

Grotzinger, J.P. and Knoll, A.H. (1999) Stromatolites in Precambrian carbonates: evolutionary mileposts or environmental dipsticks? *Annual Rev. Earth Planet. Sci.*, **27**, 313-358.

Habicht, K.S., Gade, M., Thamdrup, B., Berg, P. and Canfield, D.E. (2002) Calibration of sulfate levels in the Archean ocean. *Science*, **298**, 2372-2374.

Hawes, I., Sumner, D.Y., Andersen, D.T. and Mackey, T.J. (2011) Legacies of recent environmental change in the benthic communities of Lake Joyce, a perennially ice-covered Antarctic lake. *Geobiology*, **9**, 394-410.

Heap, M.J., Baud, P., Reuschlé, T. and Meredith, P.G. (2014) Stylolites in limestones: Barriers to fluid flow? *Geology*, **42**, 51-54.

Holland, H. D. (2002) Volcanic gases, black smokers, and the Great Oxidation Event. *Geochim. Cosmochim. Acta*, **66**, 3811-3826.

Holland, H.D. (2006) The oxygenation of the atmosphere and oceans. *Proc. Royal Soc. London B: Bio. Sci,* **361,** 903-915.

Huertas, M.J., López-Maury, L., Giner-Lamia, J., Sánchez-Riego, A.M. and Florencio, F.J. (2014) Metals in cyanobacteria: analysis of the copper, nickel, cobalt and arsenic homeostasis mechanisms. *Life*, **4**, 865-886.

Johnson, J.E., Webb, S.M., Thomas, K., Ono, S., Kirschvink, J.L. and Fischer, W.W. (2013) Manganese-oxidising photosynthesis before the rise of cyanobacteria. *Proc. Natl Acad Sci. USA*, **110**, 11238-11243.

Kamber, B.S. and Webb, G.E. (2001) The geochemistry of late Archaean microbial carbonate: implications for ocean chemistry and continental erosion history. *Geochim. Cosmochim. Acta*, **65**, 2509-2525.

Kamber, B.S. and Whitehouse, M.J. (2007). Micro-scale sulphur isotope evidence for sulphur cycling in the late Archean shallow ocean. *Geobiology*, **5**, 5-17.

Kazmierczak, J. and Altermann, W. (2002) Neoarchean biomineralization by benthic cyanobacteria. *Science*, **298**, 2351-2351.

Kazmierczak, J., Altermann, W., Kremer, B., Kempe, S. and Eriksson, P.G. (2009) Mass occurrence of benthic coccoid cyanobacteria and their role in the production of Neoarchean carbonates of South Africa. *Precamb. Res.*, **173**, 79-92.

Kirschvink, J.L. and Kopp, R.E. (2008) Palaeoproterozoic ice houses and the evolution of oxygen-mediating enzymes: the case for a late origin of photosystem II. *Proc. Royal Soc. London B: Bio. Sci*, **363**, 2755-2765.

Klein, C. (2005) Some Precambrian banded iron-formations (BIFs) from around the world: Their age, geologic setting, mineralogy, metamorphism, geochemistry, and origins. *Am. Mineral.*, **90**, 1473-1499.

Klein, C. and Beukes, N.J. (1989) Geochemistry and sedimentology of a facies transition from limestone to iron-formation deposition in the early Proterozoic Transvaal Supergroup, South Africa. *Eco. Geol.*, **84,** 1733-1774.

Klein, C., Beukes, N.J. and Schopf, J.W. (1987) Filamentous microfossils in the early Proterozoic Transvaal Supergroup: their morphology, significance, and paleoenvironmental setting. *Precamb. Res.*, **36**, 81-94.

Kretz, R. (1982) A model for the distribution of trace elements between calcite and dolomite. *Geochim. Cosmochim. Acta*, **46**, 1979-1981.

Land, L.S. (1985) The origin of massive dolomite. *Journal of Geology Education*, **33**, 112-125.

Lawrence, M.G., Greig, A., Collerson, K.D. and Kamber, B.S. (2006) Rare earth element and yttrium variability in South East Queensland waterways. *Aquatic Geochem.*, **12,** 39-72.

LeCheminant, A.N. and Heaman, L.M. (1989) Mackenzie igneous events, Canada: Middle Proterozoic hotspot magmatism associated with ocean opening. *Earth Planet. Sc. Let.,* **96**, 38-48.

Lepot, K., Benzerara, K., Brown, G.E. and Philippot, P. (2008) Microbially influenced formation of 2,724-million-year-old stromatolites. *Nature Geoscience*, **1**, 118-121.

Lepot, K., Benzerara, K., Rividi, N., Cotte, M., Brown, G.E. and Philippot, P. (2009) Organic matter heterogeneities in 2.72 Ga stromatolites: alteration versus preservation by sulfur incorporation. *Geochim. Cosmochim. Acta*, **73**, 6579-6599.

Limaye, A. (2012) Drishti: volume exploration and presentation tool. SPIE Optical Engineering+ Applications, International Society for Optics and Photonics p. 85060X. Accessed from: http://dx.doi.org/10.1117/12.935640

Luo, G., Ono, S., Beukes, N.J., Wang, D.T., Xie, S. and Summons, R.E. (2016) Rapid oxygenation of Earth's atmosphere 2.33 billion years ago. *Science Advances*, **2**, p.e1600134.

Lyons, T.W., Reinhard, C.T. and Planavsky, N.J. (2014) The rise of oxygen in Earth's early ocean and atmosphere. *Nature*, **506**, 307-315.

Machel, H.G. (2004) Concepts and models of dolomitization: a critical reappraisal, in: Braithwaite, C.J.R., Rizzi, G., Darke, G. (Eds.), The geometry and petrogenesis of dolomite hydrocarbon reservoirs. Geological Society, London, Special Publication **235**, 7-63.

Maliva, R.G., Knoll, A.H. and Siever, R. (1989) Secular change in chert distribution: a reflection of evolving biological participation in the silica cycle. *Palaios*, 519-532.

Maliva, R.G., Knoll, A.H. and Simonson, B.M. (2005) Secular change in the Precambrian silica cycle: insights from chert petrology. *Geol. Soc. Am. Bull.*, **117**, 835-845

Manning, P.L., Edwards, N.P., Wogelius, R.A., Bergmann, U., Barden, H.E., Larson, P.L., Schwarz-Wings, D., Egerton, V.M., Sokaras, D., Mori, R.A. and Sellers, W.I. (2013) Synchrotron-based chemical imaging reveals plumage patterns in a 150 million year old early bird. *Jour. Anal. Atomic Spectro.*, **28**, 1024-1030.

Manning-Berg, A.R. and Kah, L.C. (2017) Proterozoic microbial mats and their constraints on environments of silicification. *Geobiology*, **15**, 469-483.

Martin, D.M., Clendenin, C.W., Krapez, B. and McNaughton, N.J. (1998) Tectonic and geochronological constraints on late Archaean and Palaeoproterozoic stratigraphic correlation within and between the Kaapvaal and Pilbara Cratons. *Jour. Geol. Soc.*, **155**, 311-322.

Meyer, N.R., Zerkle, A.L. and Fike, D.A. (2017) Sulphur cycling in a Neoarchaean microbial mat. *Geobiology*, **15**, 353-365.

Morrow, D.W. and Ricketts, B.D. (1988). Experimental investigation of sulfate inhibition of dolomite and its mineral analogues. In: Shukla, V. and. Baker, P.A (Eds.), Sedimentology and Geochemistry of Dolostones, Soc. Econ. Paleont. Mineralog, 25-38

Morse, J. W., Bender, M. L. (1990) Partition coefficients in calcite: Examination of factors influencing the validity of experimental results and their application to natural systems. *Chem. Geol.*, 82, 265-277.

Murphy, M.A. and Sumner, D.Y. (2008) Variations in Neoarchean microbialite morphologies: clues to controls on microbialite morphologies through time. *Sedimentology*, **55**, 1189-1202.

Petrash, D.A., Lalonde, S.V., González-Arismendi, G., Gordon, R.A., Méndez, J.A., Gingras, M.K. and Konhauser, K.O. (2015) Can Mn–S redox cycling drive sedimentary dolomite formation? A hypothesis. *Chem. Geol.*, **404**, 27-40.

Phoenix, V.R., Konhauser, K.O. and Ferris, F.G. (2003) Experimental study of iron and silica immobilization by bacteria in mixed Fe–Si systems: implications for microbial silicification in hot springs. *Can. J. Earth Sci.,* **40**, 1669-1678.

Rasmussen, B., Blake, T.S. and Fletcher, I.R. (2005) U-Pb zircon age constraints on the Hamersley spherule beds: Evidence for a single 2.63 Ga Jeerinah-Carawine impact ejecta layer. *Geology*, **33**, 725-728.

Rasmussen, B., Fletcher, I.R., Brocks, J.J. and Kilburn, M.R. (2008) Reassessing the first appearance of eukaryotes and cyanobacteria. *Nature*, **455**, 1101-1104.

Raven, J.A., Evans, M.C. and Korb, R.E. (1999) The role of trace metals in photosynthetic electron transport in O2-evolving organisms. *Photosynth. Res.*, **60**, 111-150.

Schirrmeister, B. E., Sanchez-Baracaldo, P., and Wacey, D. (2016) Cyanobacterial evolution during the Precambrian. *Int. Jour. Astrobio*, 1-18. doi: 10.1017/S1473550415000579.

Schröder, S., Lacassie, J.P. and Beukes, N.J. (2006) Stratigraphic and geochemical framework of the Agouron drill cores, Transvaal Supergroup (Neoarchean–Paleoproterozoic, South Africa). *S. African Jour. Geol.*, **109**, 23-54.

Schröder, S., Beukes, N.J. and Sumner, D.Y. (2009) Microbialite–sediment interactions on the slope of the Campbellrand carbonate platform (Neoarchean, South Africa). *Precamb. Res.*, **169**, 68-79.

Sforna, M.C., Philippot, P., Somogyi, A., van Zuilen, M.A., Medjoubi, K., Schoepp-Cothenet, B., Nitschke, W. and Visscher, P.T. (2014) Evidence for arsenic metabolism and cycling by microorganisms 2.7 billion years ago. *Nature Geoscience*, **7**, 811-815.

Sforna, M.C., Daye, M., Philippot, P., Somogyi, A., Zuilen, M.A., Medjoubi, K., Gérard, E., Jamme, F., Dupraz, C., Braissant, O. and Glunk, C., (2017) Patterns of metal distribution in hypersaline microbialites during early diagenesis: Implications for the fossil record. *Geobiology*, **15**, 259-279.

Shcolnick, S. and Keren, N. (2006) Metal homeostasis in cyanobacteria and chloroplasts. Balancing benefits and risks to the photosynthetic apparatus. *Plant physiology*, **141**, 805-810.

Shepard, R.N. and Sumner, D.Y. (2010) Undirected motility of filamentous cyanobacteria produces reticulate mats. *Geobiology*, **8**, 179-190.

Siever, R. (1992) The silica cycle in the Precambrian. *Geochim. Cosmochim. Acta*, **56**, 3265-3272.

Solé, V.A., Papillon, E., Cotte, M., Walter, P. and Susini, J. (2007) A multiplatform code for the analysis of energy-dispersive X-ray fluorescence spectra. *Spectrochim. Acta B: Atomic Spectro.*, **62**, 63-68.

Streng, M., Butler, A.D., Peel, J.S., Garwood, R.J. and Caron, J.B. (2016) A new family of Cambrian rhynchonelliformean brachiopods (Order Naukatida) with an aberrant coral-like morphology. *Palaeontology*, **59**, 269-293.

Summons, R.E., Jahnke, L.L., Hope, J.M. and Logan, G.A. (1999) 2-Methylhopanoids as biomarkers for cyanobacterial oxygenic photosynthesis. *Nature*, **400**, 554-557.

Sumner, D.Y. (1997). Late Archean calcite-microbe interactions; two morphologically distinct microbial communities that affected calcite nucleation differently. *Palaios*, **12**, 302-318.

Sumner, D.Y. (2000). Microbial vs environmental influences on the morphology of Late Archean fenestrate microbialites. In: Riding, R.E. and Awramik, S.M. (Eds) *Microbial Sediments*. Springer Berlin Heidelberg, pp. 307-314.

Sumner, D.Y. and Beukes, N.J. (2006) Sequence stratigraphic development of the Neoarchean Transvaal carbonate platform, Kaapvaal Craton, South Africa. *S. African Jour. Geol.*, **109**, 11-22.

Sumner, D.Y. and Bowring, S.A. (1996) U-Pb geochronologic constraints on deposition of the Campbellrand Subgroup, Transvaal Supergroup, South Africa. *Precamb. Res.*, **79**, 25-35.

Sumner, D.Y. and Grotzinger, J.P. (1996) Herringbone calcite: petrography and environmental significance. *Jour. Sed. Res.*, **66**, 419-429.

Sumner, D.Y. and Grotzinger, J.P. (2004) Implications for Neoarchaean ocean chemistry from primary carbonate mineralogy of the Campbellrand-Malmani Platform, South Africa. *Sedimentology*, **51**, 1273-1299.

Sumner, D.Y., Hawes, I., Mackey, T.J., Jungblut, A.D. and Doran, P.T. (2015) Antarctic microbial mats: A modern analog for Archean lacustrine oxygen oases. *Geology*, **43**, 887-890.

Sumner, D.Y., Jungblut, A.D., Hawes, I., Andersen, D.T., Mackey, T.J. and Wall, K. (2016) Growth of elaborate microbial pinnacles in Lake Vanda, Antarctica. *Geobiology*, **14**, 556-574.

Sverjensky, D.A. (1987) Calculation of the thermodynamic properties of aqueous species and the solubilities of minerals in supercritical electrolyte solutions. In: Carmichael, I.S.E. and Eugster, H.P. (Eds.) Thermodynamics of Earth Materials. *Rev. Mineral. Geochem.*, **17**, 177-20

van Lith, Y., Warthmann, R., Vasconcelos, C. and McKenzie, J.A. (2003a) Microbial fossilization in carbonate sediments: a result of the bacterial surface involvement in dolomite precipitation. *Sedimentology*, **50**, 237-245.

van Lith, Y., Warthmann, R., Vasconcelos, C. and Mckenzie, J.A. (2003b) Sulphate-reducing bacteria induce low-temperature Ca-dolomite and high Mg-calcite formation. *Geobiology*, **1**, 71-79.

Vasconcelos, C. and McKenzie, J.A. (1997) Microbial mediation of modern dolomite precipitation and diagenesis under anoxic conditions (Lagoa Vermelha, Rio de Janeiro, Brazil). *Jour. Sed Res*, **67**, 378-390.

Vasconcelos, C., McKenzie, J.A., Bernasconi, S., Grujic, D. and Tiens, A.J. (1995) Microbial mediation as a possible mechanism for natural dolomite formation at low temperatures. *Nature*, **377**, 220-222.

Vasconcelos, C., Warthmann, R., McKenzie, J.A., Visscher, P.T., Bittermann, A.G. and van Lith, Y. (2006) Lithifying microbial mats in Lagoa Vermelha, Brazil: modern Precambrian relics? *Sed. Geol.*, **185**, 175-183.

Veizer, J. (1983) Chemical diagenesis of carbonates: theory and application of trace element technique. In: Arthur, M. A., Anderson, T. F., Kaplan, I. B., Veizer, J. (Eds) Stable isotopes in sedimentary geology. SEPM Short Course Notes 10, 3-1 – 3-100.

Voegelin, A.R., Nägler, T.F., Beukes, N.J. and Lacassie, J.P. (2010) Molybdenum isotopes in late Archaean carbonate rocks: Implications for Early Earth oxygenation. *Precamb. Res.*, **182**, 70-82.

Warke, M.R., Schröder, S. and Strauss, H. (2018) Testing models of pre-GOE environmental oxidation: A Paleoproterozoic marine signal in platform dolomites of the Tongwane Formation (South Africa). *Precamb. Res.*, **313**, 205-220.

Warthmann, R., Van Lith, Y., Vasconcelos, C., McKenzie, J.A. and Karpoff, A.M. (2000) Bacterially induced dolomite precipitation in anoxic culture experiments. *Geology*, **28**, 1091-1094.

Winkel, L.H., Casentini, B., Bardelli, F., Voegelin, A., Nikolaidis, N.P. and Charlet, L. (2013) Speciation of arsenic in Greek travertines: Co-precipitation of arsenate with calcite. *Geochim. Cosmochim. Acta*, **106**, 99-110.

Wille, M., Kramers, J.D., Nägler, T.F., Beukes, N.J., Schröder, S., Meisel, Th., Lacassie, J.P. and Voegelin, A.R. (2007) Evidence for a gradual rise of oxygen between 2.6 and 2.5 Ga from Mo isotopes and Re-PGE signatures in shales. *Geochim. Cosmochim. Acta*, **71**, 2417-2435.

Webster-Brown, J.G. and Webster, K.S., (2007) Trace metals in cyanobacterial mats, phytoplankton and sediments of the Lake Vanda region, Antarctica. *Antarctic Science*, **19**, 311-319.

Wogelius, R.A. and Walther, J.V. (1991) Olivine dissolution at 25 C: Effects of pH, CO2, and organic acids. *Geochim. Cosmochim. Acta*, **55**, 943-954.

Wogelius, R.A., Manning, P.L., Barden, H.E., Edwards, N.P., Webb, S.M., Sellers, W.I., Taylor, K.G., Larson, P.L., Dodson, P., You, H. and Da-Qing, L. (2011) Trace metals as biomarkers for eumelanin pigment in the fossil record. *Science*, **333**, 1622-1626.

Wright, D.T. (2000) Benthic microbial communities and dolomite formation in marine and lacustrine environments—a new dolomite model. *Marine Authigenesis: From Global to Microbial. SEPM Special Publication*, **66**, 7-20.

Wright, D.T. and Altermann, W. (2000) Microfacies development in Late Archaean stromatolites and oolites of the Ghaap Group of South Africa. *Geol. Soc. London, Special Publications*, **178**, 51-70.

Zhelezinskaia, I., Kaufman, A.J., Farquhar, J. and Cliff, J. (2014) Large sulfur isotope fractionations associated with Neoarchean microbial sulfate reduction. *Science*, **346**, 742-744.

Figure captions

Figure 1: Regional map of the Neoarchean-Palaeoproterozoic Transvaal Supergroup as preserved in the Transvaal and Griqualand West basins in South Africa. West of Griquatown the position of core GKF01 (from which sample was obtained) is indicated. Modified after Sumner and Grotzinger (2004).

Figure 2: Stratigraphic column of the lower Transvaal Supergroup as preserved in the Griqualand West Basin; the Gamohaan Formation is indicated. Absolute age constraints are provided by Sumner and Bowring (1996), Altermann and Nelson (1998), Pickard (2003) and Gutzmer and Beukes (1998).

Figure 3: Images of cuspate stromatolites (dolomite) exposed on the farm Gladstone near Daniëlskuil: (A) profile view, showing distinct vertical elements (green) which are attached to inclined to subhorizontal elements (yellow), and which pass into rolled up/distorted elements; (B) sketch showing the component parts of a cuspate stromatolite, adapted from Sumner (2000); (C) plan view, stromatolites (yellow, dashed) are linked by sub-linear structures (green, dashed) which may have constituted ridges. In both photographs white areas correspond to patches of calcite cement.

Figure 4: Sample GAM in blocks GAM1A (upper) and GAM1B (lower) in bedding orientation; the sample blocks are separated by a fracture. Cyclical textures of contorted laminae layers (CL) and growth layers (GL) and examples of drape, support and contorted laminae textures are indicated. Drill sites for XRD and ICP-MS/AES analysis are indicated with white dots and were sampled from the counterpart of the sample pictured. SRS-XRF scans correspond to the box indicated. Scale bar = 17 cm.

Figure 5: plane polarized and cross-polarized transmitted light images of microtextures observed in thin section with area od sample imaged in parentheses – i.e. growth layer 1 (GL1) and contorted laminae layer 1 (CL1): (A) dark-green stained, finely crystalline, xenotopic, ferroan dolospar in biogenic contorted laminae layers which are encased within equigranular purple stained ferroan calcite cement (CL1); (B) cubic opaque minerals spatially restricted to dolomitic, biogenic S structure with upward growth in direction of arrow (GL1); (C) roll-up of mat structures (CL1); (D) roll-up and peloid structures (CL1); (E) support and drape structures, showing steep inclination of drapes near to support structures (GL1); (F) thin, inclined drapes bifurcate and thicken during transition to sub-horizontal orientations (GL1). Scale bar = 200 µm (B, C) or 500 µm (A, D, E, F).

Figure 6: plane polarized and cross-polarized transmitted light images of microtextures observed in thin section with area od sample imaged in parentheses – i.e. growth layer 1 (GL1) and contorted laminae layer 1 (CL1): (A) ferroan calcite cements precipitated within microbial

roll-ups (CL1); (B) herring-bone calcite textures with crystal long axes orientated perpendicularly to support structures (GL1); (C) silica spherules with radial growth patterns (GL1); (D) localized silicification textures (GL1); (E) stylolite cross-crossing drape structures (GL1); (F) bifurcating stylolite that forms boundary between CL1 and GL1. Scale bar = 500 µm in all images.

Figure 7: PAAS-normalized REY_{SN} patterns showing characteristics consistent of authigenic carbonate which has precipitated from Neoarchean seawater.

Figure 8: SRS-XRF element distribution maps of heavier elements analyzed under an incident beam energy of 13.5 keV. All maps are clipped at 98 % except Zn which is clipped at 99.9 %. Labelled features: (1) stylolites, (2) zoned lunate calcite cements, (3) support structures, (4) drapes. Growth layers are marked GL and contorted laminae layers as CL.

Figure 9: SRS-XRF element distribution maps of lighter elements analyzed under an incident beam energy of 3.15 keV. Labelled features as Figure 8: (1) stylolites, (2) zoned lunate calcite cements, and (5) silica spherules. Growth layers are marked GL and contorted laminae layers as CL.

Figure 10: XMT image of bottom part of GAM1A (upper portion of sample) showing: (left) spatial association of stylolite with sub-vertical structures (veinlets) which thin upwards; (right) magnified image showing quartz spherules connected to sub-vertical structure which is probably a veinlet infilled by silica.
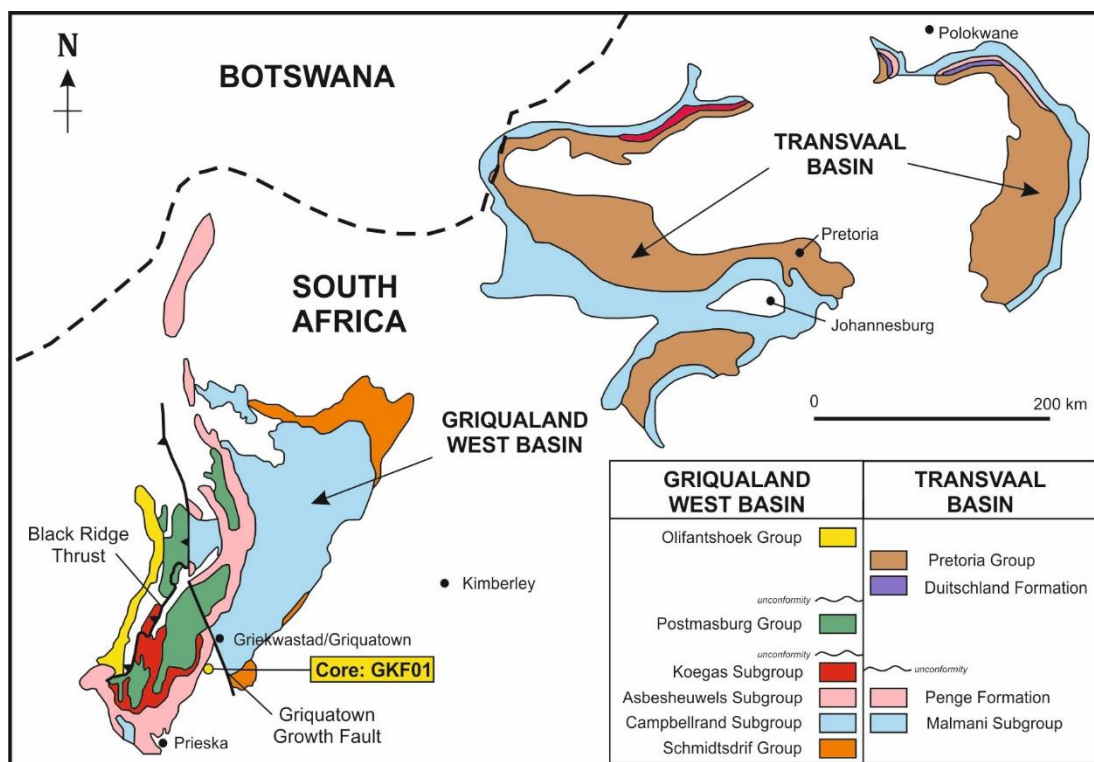
Figure 1: Regional map of the Neoarchean-Palaeoproterozoic Transvaal Supergroup as preserved in the Transvaal and Griqualand West basins in South Africa. West of Griquatown the position of core GKF01 (from which sample was obtained) is indicated.
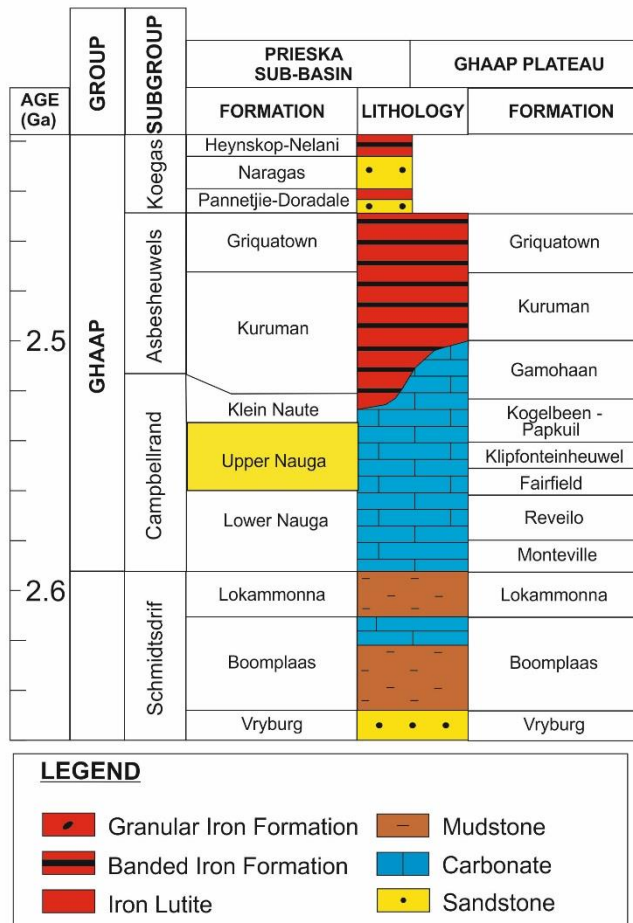

Figure 2: Stratigraphic column of the lower Transvaal Supergroup as preserved in the Griqualand West Basin; the Gamohaan Formation is indicated. Absolute age constraints are provided by Sumner and Bowring (1996), Altermann and Nelson (1998), Pickard (2003) and Gutzmer and Beukes (1998).
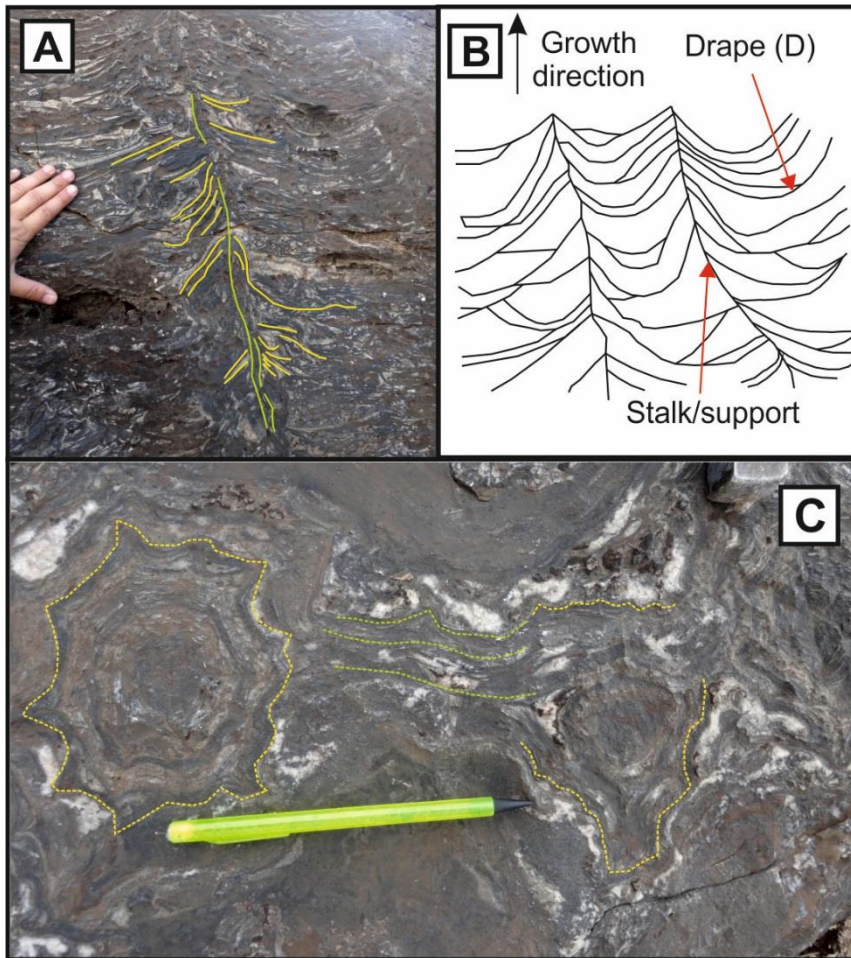
Figure 3: Images of cuspate stromatolites (dolomite) exposed on the farm Gladstone near Daniëlskuil: (A) profile view, showing distinct vertical elements (green) which are attached to inclined to subhorizontal elements (yellow), and which pass into rolled up/distorted elements; (B) sketch showing the component parts of a cuspate stromatolite, adapted from Sumner (2000); (C) plan view, stromatolites (yellow, dashed) are linked by sublinear structures (green, dashed) which may have constituted ridges. In both photographs white areas correspond to patches of calcite cement.
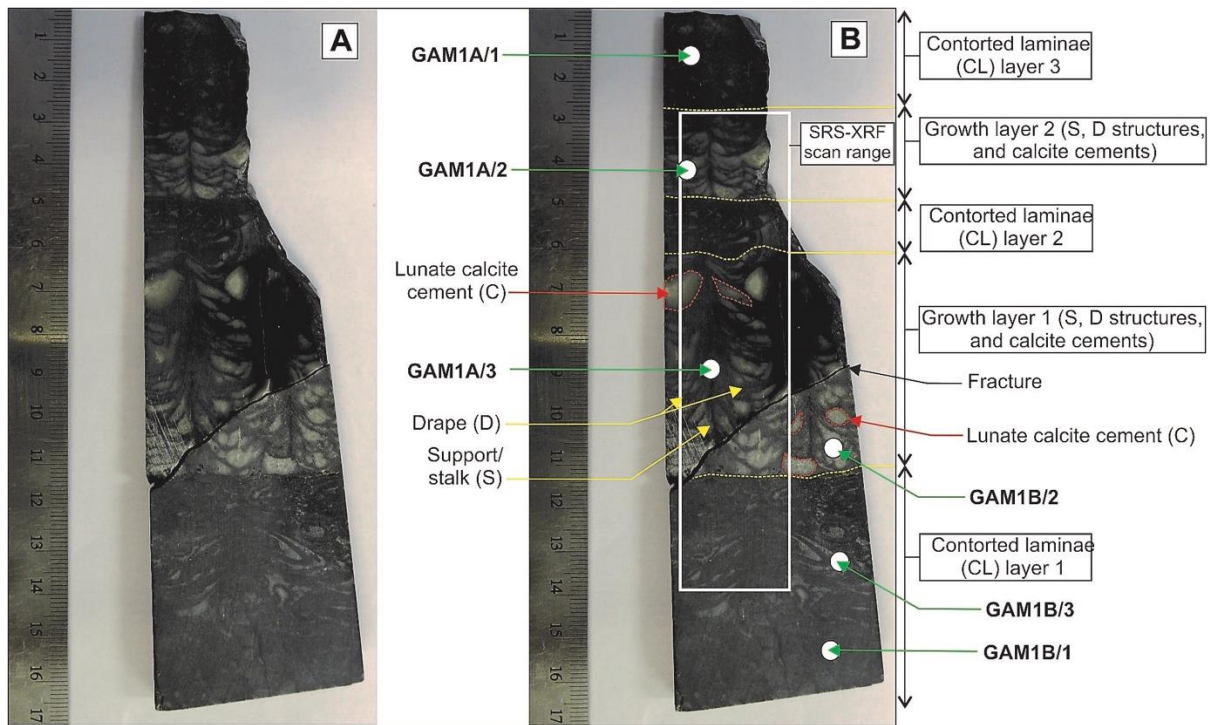
Figure 4: Sample GAM in blocks GAM1A (upper) and GAM1B (lower) in bedding orientation; the sample blocks are separated by a fracture. Cyclical textures (CL and growth layers) and examples of D, S and C textures are indicated. Drill sites for XRD and ICP-MS/AES analysis are indicated with white dots and were sampled from the counterpart of the sample pictured. SRS-XRF scans correspond to the box indicated. Scale bar = 17 cm.
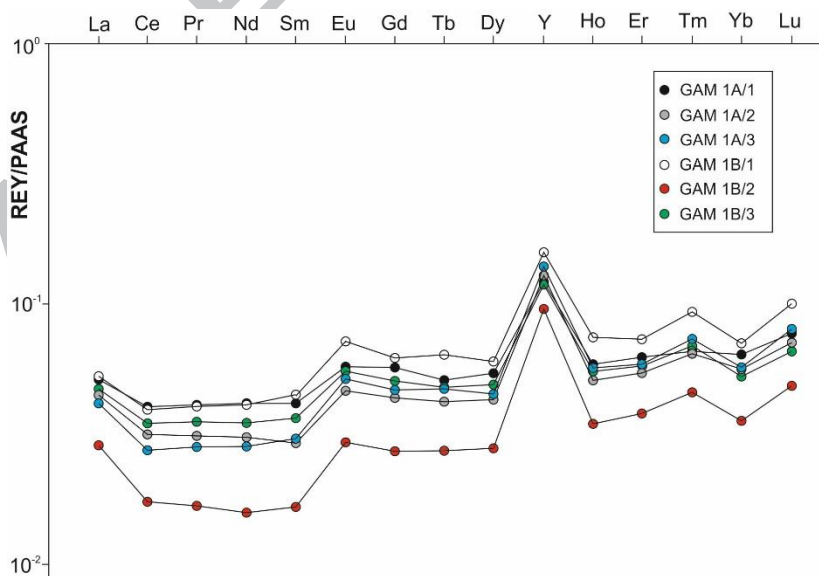

Figure 8: PAAS-normalized REY$_{SN}$ patterns showing characteristics consistent of authigenic carbonate which has precipitated from Neoarchean seawater.
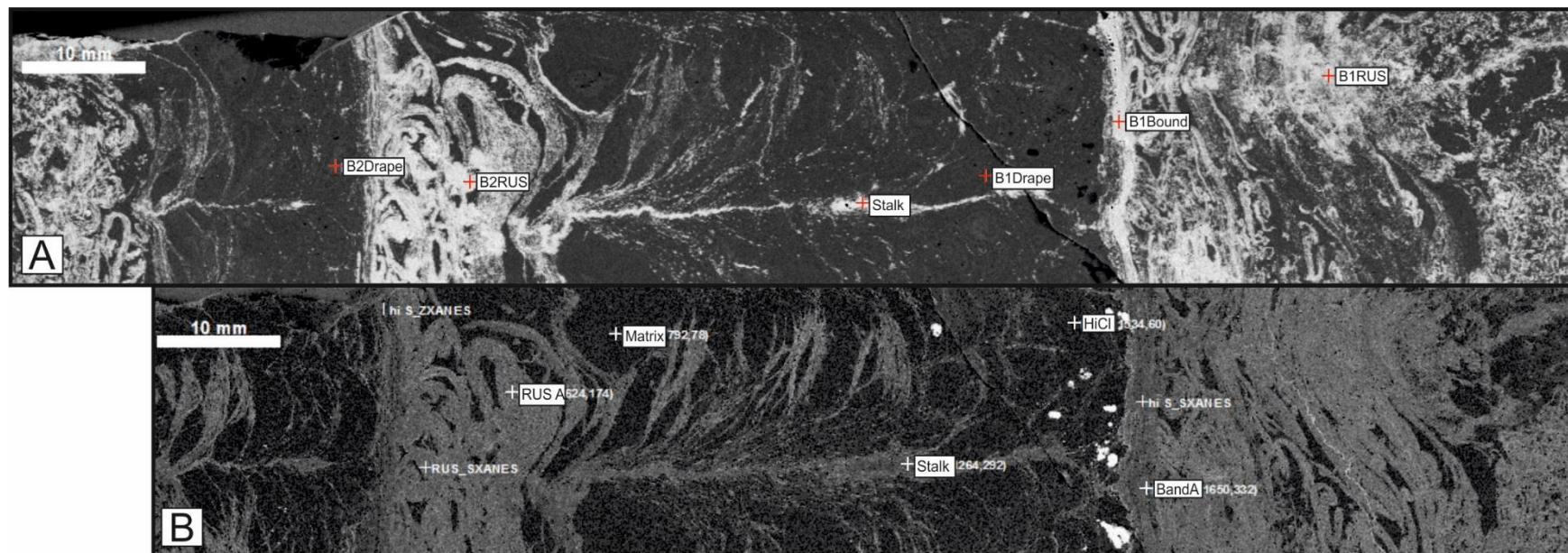
Figure 5: location of point analyses from scans conducted with incident beam energy of: (A) 13.5 keV (Fe) and (B) 3.15 keV (Al). Scale bar = 10 mm.
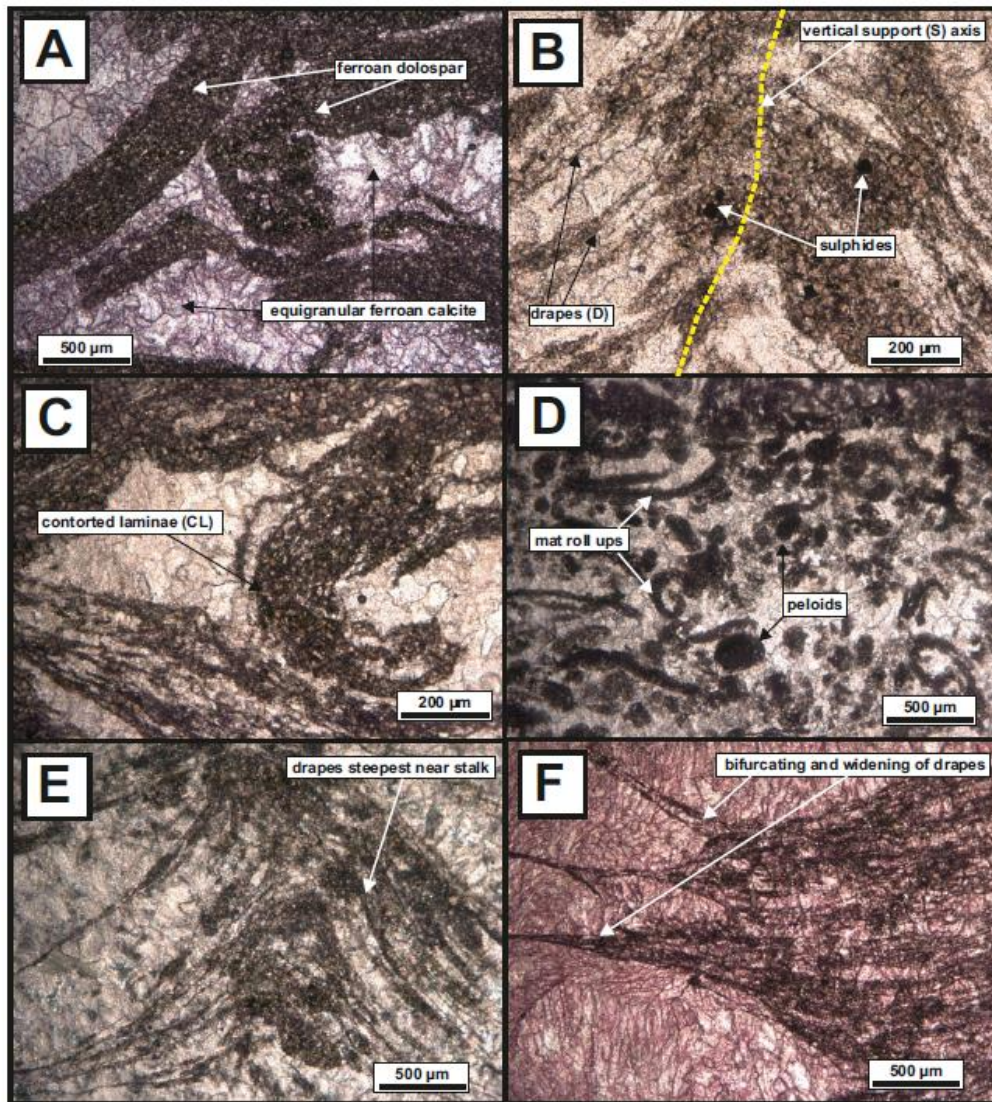
Figure 6: plane polarized (PPL) and cross-polarixed (XPL) transmitted light images of microtextures observed in thin section: **(A)** dark-green stained, finely crystalline, xenotopic, ferroan dolospar in biogenic CL layers which are encased within equigranular purple stained ferroan calcite cement; **(B)** cubic opaque minerals spatially restricted to dolomitic, biogenic S structure; **(C)** roll-up of mat structures; **(D)** roll-up and peloid structures; **(E)** S and D structures, showing steep inclination of drapes near to support structures; **(F)** thin, inclined drapes bifurcate and thicken during transition to sub-horizontal orientations. Scale bar = 200 μm (B, C) or 500 μm (A, D, E, F).
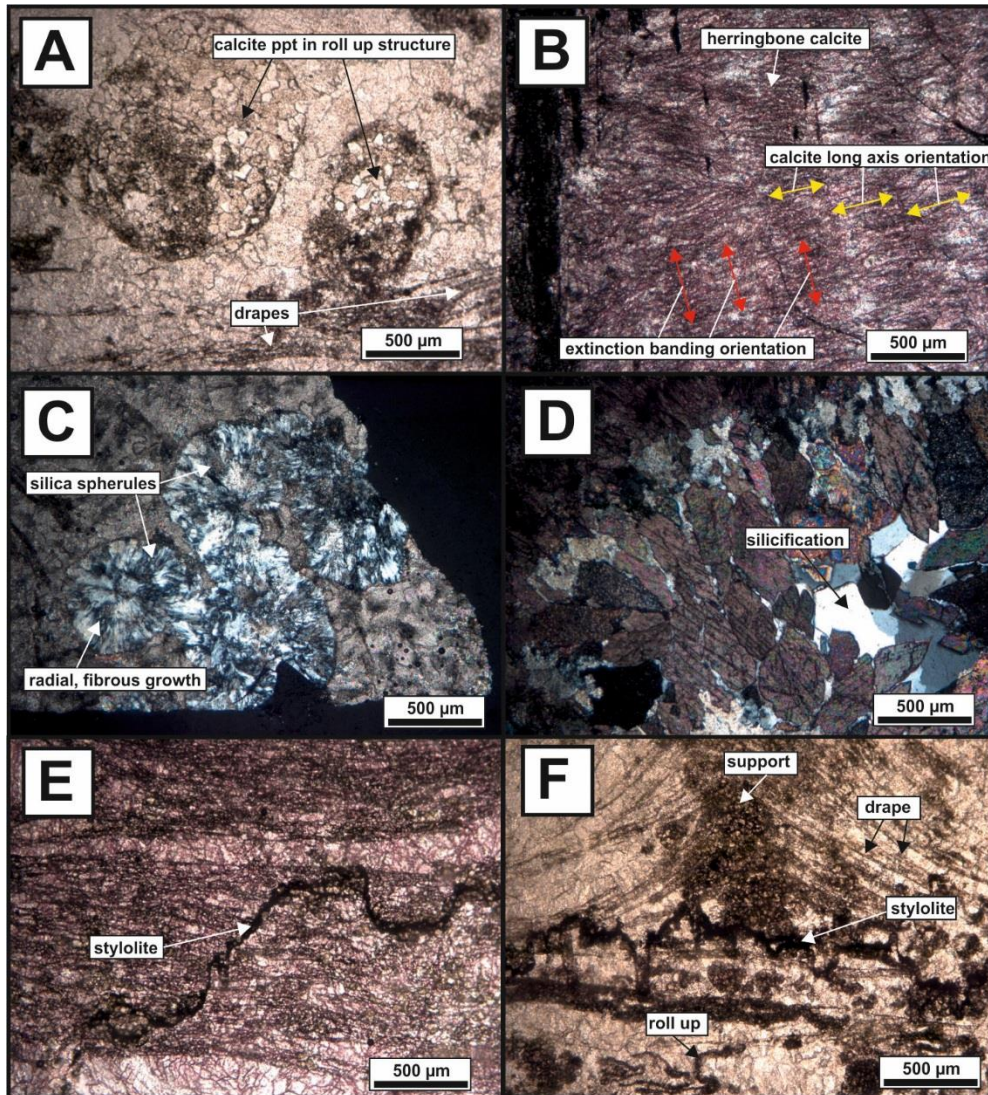
Figure 7: plane polarized (PPL) and cross-polarixed (XPL) transmitted light images of microtextures observed in thin section: (A) ferroan calcite cements precipitated within microbial roll-ups; (B) herring-bone calcite textures with crystal long axes orientated perpendicularly to S structures; (C) silica spherules with radial growth patterns; (D) localized silicification textures; (E) stylolite cross-crossing drape structures; (F) bifurcating stylolite that forms boundary between CL layer 1 and growth layer 1. Scale bar = 500 μm in all images.

Sample	Dominant mineralogy	Trace Element (ppm unless stated otherwise)								Mineralogy (XRD)
		Sr	Mn	Ca (%)	Fe	Mg (%)	Ti	Th	Al	
GAM 1A/1	DOLO(F)	27	9120	32.8	6705	2.8	3.2	0.4	390	dolomite, calcite, quartz
GAM 1A/2	CALC(F)	30	7318	36.7	3038	1.0	1.1	0.2	110	dolomite, calcite, quartz
GAM 1A/3	CALC(F)	26	7701	37.1	3052	1.1	1.9	0.5	254	dolomite, calcite, quartz
GAM 1B/1	DOLO(F)	27	9758	32.7	6982	2.9	3.9	0.9	556	dolomite, calcite, quartz
GAM 1B/2	CALC(F)	28	7242	40.0	1619	0.2	0.4	0.2	41	dolomite, calcite, quartz
GAM 1B/3	DOLO(F)	32	9904	32.3	6962	2.9	3.4	0.6	496	dolomite, calcite, quartz

Table 1: carbonate bound element concentrations within sample and phases identified using XRD. 'DOLO(F)' refers to ferroan dolomite dominated sites, 'CALC(F)' to ferroan calcite dominated sites. XRD spectra are included in the SI.

Sample	La	Ce	Pr	Nd	Sm	Eu	Gd	Tb	Dy	Y	Ho	Er	Tm	Yb	Lu	ΣREE	Y/Ho
PAAS	38	80	8.9	32	5.6	1.1	4.7	0.77	4.4	27	1	2.9	0.4	2.8	0.43	210	27
GAM 1A/1	1.96	3.21	0.36	1.32	0.23	0.06	0.27	0.04	0.24	3.40	0.06	0.18	0.03	0.18	0.03	11.57	58.78
GAM 1A/2	1.70	2.52	0.28	0.98	0.16	0.05	0.21	0.03	0.19	3.40	0.05	0.16	0.03	0.15	0.03	9.94	66.86
GAM 1A/3	1.59	2.19	0.25	0.91	0.17	0.06	0.22	0.04	0.20	3.78	0.06	0.17	0.03	0.16	0.03	9.85	66.57
GAM 1B/1	2.01	3.14	0.36	1.32	0.25	0.08	0.29	0.05	0.26	4.24	0.07	0.21	0.04	0.20	0.04	12.56	57.33
GAM 1B/2	1.08	1.39	0.15	0.51	0.09	0.03	0.13	0.02	0.12	2.58	0.03	0.11	0.02	0.10	0.02	6.39	75.08
GAM 1B/3	1.78	2.77	0.31	1.11	0.20	0.06	0.24	0.04	0.21	3.20	0.06	0.17	0.03	0.15	0.03	10.36	58.01

Table 2: REE concentrations and Y/Ho ratios. The dominant mineralogy of each sample is shown in Table 1.

		HZ Element concentration (peak fitting error)							
Element (% or ppm)	Ca (%)	Mn (%)	Fe (%)	Fe (ppm)	Zn (ppm)	Ga (ppm)	As (ppm)	Cu (ppm)
B1Bound	21.8 (2.6)	4.3 (0.2)	4.7 (0.2)		71.8 (8.8)	0.8 (0.2)	12.1 (1.8)	n.d.
B1Drape	50.8 (5.4)	1.2 (0.1)		3216.7 (274.0)	108.0 (12.4)	n.d.	4.3 (0.8)	n.d.
B1RUS	24.8 (2.9)	3.1 (0.2)	3.5 (0.2)		65.4 (8.3)	2.8 (0.5)	9.4 (1.5)	n.d.
B2Drape	50.7 (5.4)	1.4 (0.1)		3181.3 (272.0)	61.6 (8.2)	n.d.	5.8 (1.0)	n.d.
B2RUS	27.7 (3.2)	3.2 (0.2)	3.6 (0.2)		78.0 (9.6)	1.9 (0.4)	9.5 (1.5)	2.0 (0.4)
Stalk	23.2 (2.7)	4.0 (0.2)	5.3 (0.2)		71.9 (8.8)	1.0 (0.2)	82.7 (7.0)	20.0 (2.8)
		LZ Element concentration (peak fitting error)							
Element (ppm)	Si	P	S	Cl				
BandA	8188.1 (722.5)	431.1 (57.4)	505.7 (57.9)	439.2 (45.9)				
HighCl	2212.3 (260.7)	328.7 (45.4)	481 (55.3)	732.9 (69.1)				
Matrix	1338.2 (178.1)	240.5 (35.5)	285.0 (35.8)	424.8 (45.0)				
RUSA	5699.2 (561.0)	329.2 (47.0)	267.5 (34.8)	321.6 (36.2)				
Stalk	7812.7 (766.2)	338.4 (47.6)	291.9 (37.4)	385.0 (42.1)				

Table 3: element concentrations determined from SRS-XRF point analyses. Location of point analyses are shown in Figure 5.
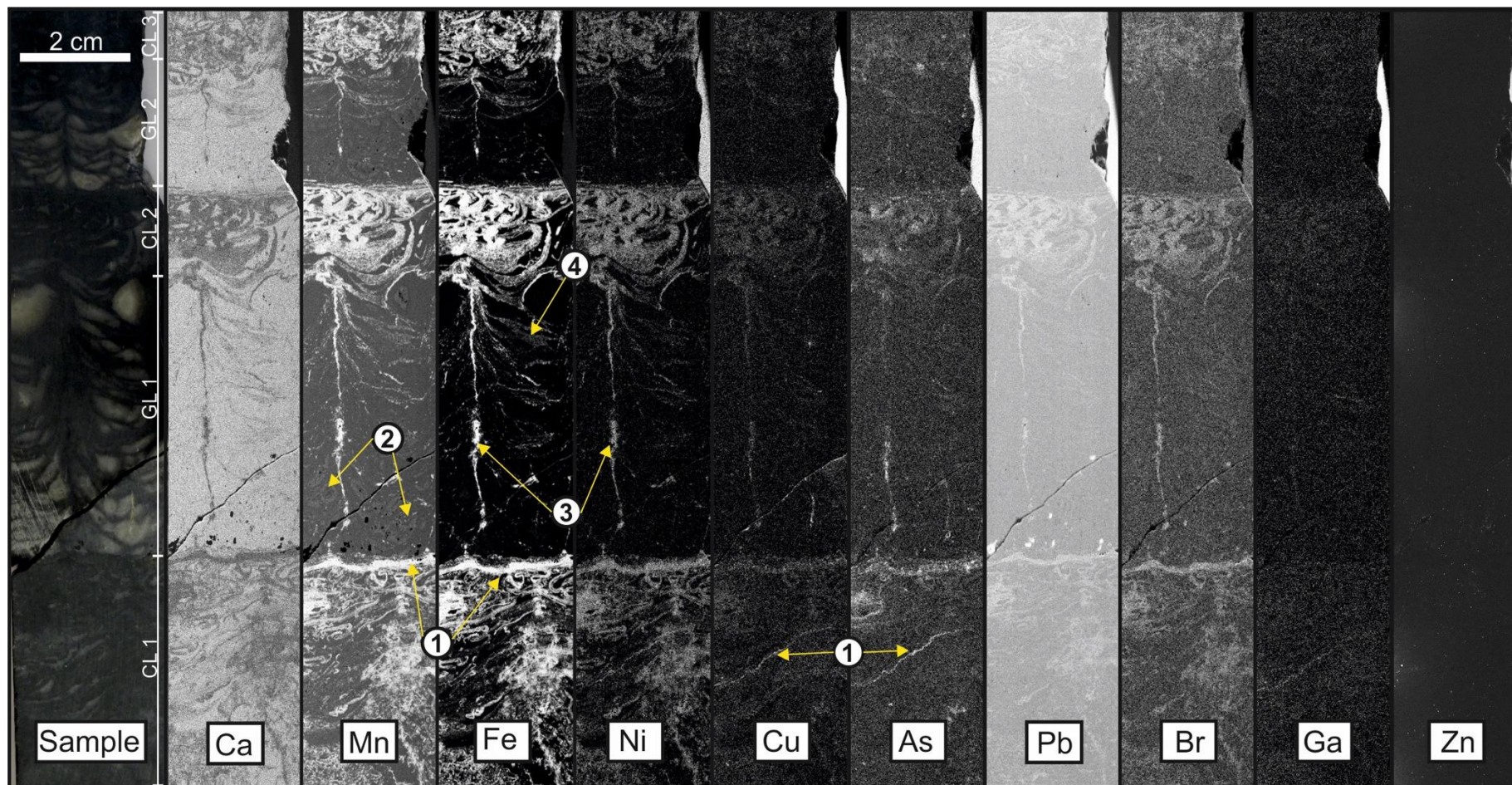
Figure 9: SRS-XRF element distribution maps of heavier elements analyzed under an incident beam energy of 13.5 keV. Labelled features: (1) stylolites, (2) zoned lunate cements (L-structures), (3) stalk/support (S-structures), (4) drapes (D-structures).
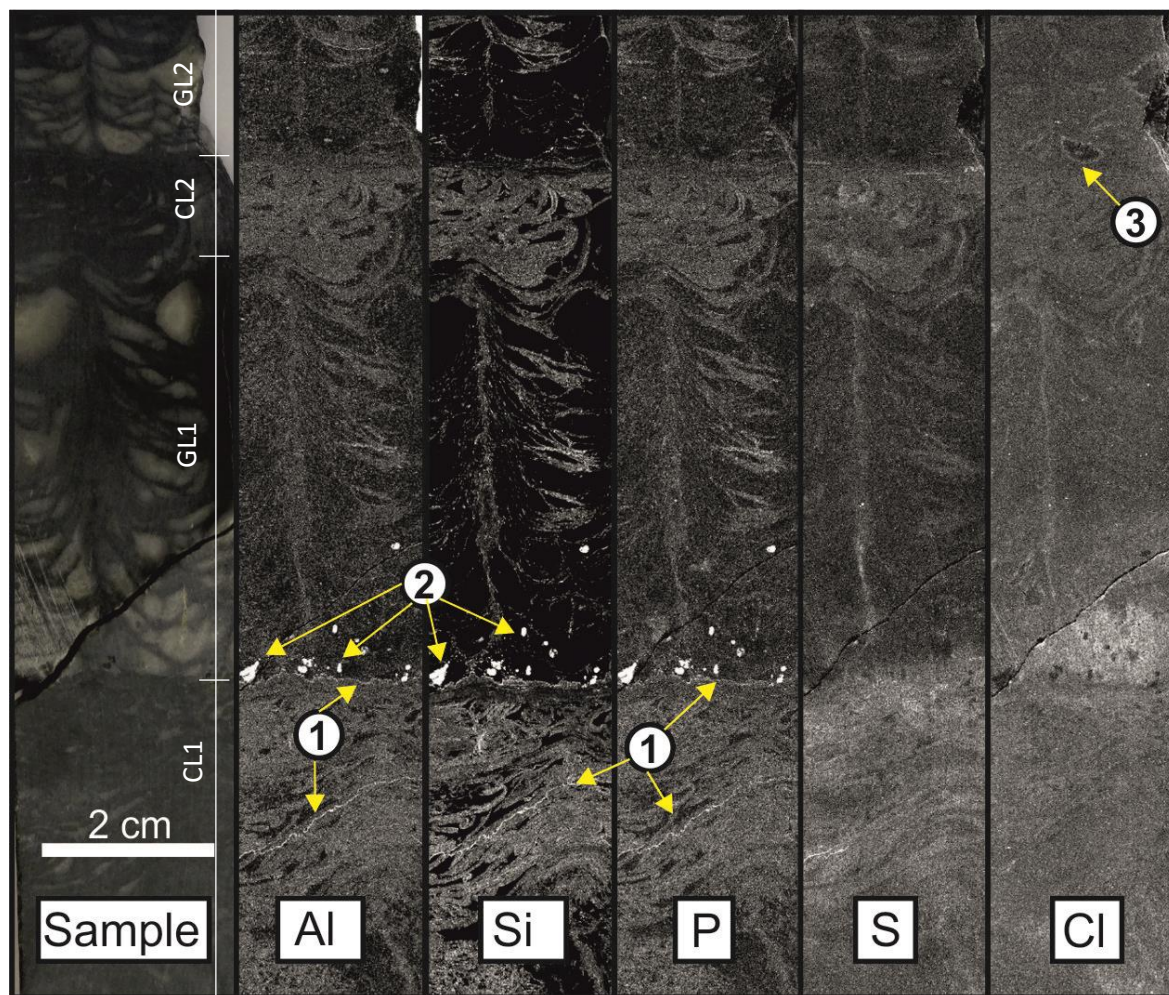
Figure 10: SRS-XRF element distribution maps of lighter elements analyzed under an incident beam energy of 3.15 keV. Labelled features: (1) stylolites, (2) silica spherules, (3) zoned lunate calcite cement (L-structure).
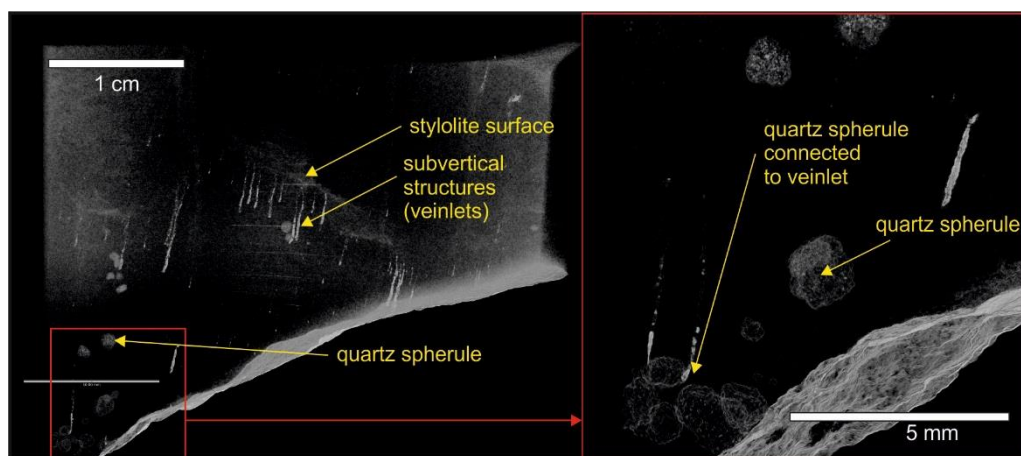
Figure 11: XMT image of bottom part of GAM1A (upper portion of sample) showing: (left) spatial association of stylolite with sub-vertical structures (veinlets) which thin upwards; (right) magnified image showing quartz spherules connected to sub-vertical structure which is probably a veinlet infilled by silica.